Improving Antarctic Bottom Water precursors in NEMO for climate applications

Katherine Hutchinson [1], Julie Deshayes [1], Christian Éthé [1], Clément Rousset [1], Casimir de Lavergne [1], Martin Vancoppenolle [1], Nicolas C. Jourdain [2], and Pierre Mathiot [2]

[1] LOCEAN Laboratory, Sorbonne Université CNRS-IRD-MNHN, Paris, France

[2] Univ. Grenoble Alpes/CNRS/IRD/G-INP, IGE, Grenoble, France

Correspondence to: Katherine Hutchinson (kath.hutchinson@gmail.com)

Abstract. The world's largest ice shelves are found in the Antarctic Weddell and Ross Seas where complex interactions between the atmosphere, sea ice, ice shelves and ocean transform shelf waters into High Salinity Shelf Water (HSSW) and Ice Shelf Water (ISW), the parent waters of Antarctic Bottom Water (AABW). This process feeds the lower limb of the global overturning circulation as AABW, the world's densest and deepest water-mass, spreads outwards from Antarctica. None of the coupled climate models contributing to CMIP6 directly simulated ocean-ice shelf interactions, thereby omitting a potentially critical piece of the climate puzzle. As a first step towards better representing these processes in a global ocean model, we run a 1° resolution forced configuration of NEMO (eORCA1) to explicitly simulate circulation beneath Filchner-Ronne (FRIS), Larsen C (LCIS), and Ross (RIS) ice shelves. These locations are thought to supply the majority of the source waters for AABW and so melt in all other cavities is provisionally prescribed. Results show that the grid resolution of 1° is sufficient to produce melt rate patterns and total melt fluxes of FRIS (117 ± 21 Gt/yr), LCIS (36 ± 7 Gt/yr) and RIS (112 ± 22 Gt/yr) that agree well with both high resolution models and satellite measurements. Most notably, allowing sub-ice shelf circulation reduces salinity biases (0.1 psu), produces the previously unresolved water mass ISW, and re-organises the shelf circulation to bring the regional model hydrography closer to observations. A change in AABW within the Weddell and Ross Seas towards colder, fresher values is identified but the magnitude is limited by the absence of a realistic overflow. This study presents a NEMO configuration that can be used for climate applications with improved realism of the Antarctic continental shelf circulation and a better representation of the precursors of AABW.

Plain language summary. Bottom Water constitutes the bottom half of the ocean's overturning system and is primarily formed in the Antarctic Weddell and Ross Seas due to interactions between the atmosphere, ocean, sea ice and ice shelves. Here we use a global ocean 1° resolution model with explicit representation of the three large ice shelves important for the formation of the parent waters of Bottom Water. We find doing so reduces salt biases, improves water mass realism, and gives realistic ice shelf melt rates.

1 Introduction

The Southern Ocean plays a vital role in global ocean circulation and in the storage of both heat and carbon (Marshall and Speer, 2012; Frölicher et al., 2015; Rintoul, 2018). Within this backdrop, the processes taking place adjacent to and underneath the Antarctic ice shelves are not only important for controlling regional ocean dynamics but also for facilitating globally important water mass transformations (Schodlok et al., 2015). Sea ice formation on the continental shelf decreases the buoyancy of the underlying waters through the process of brine rejection creating High Salinity Shelf Water (HSSW; Jacobs et al., 1979). When this dense water mass is formed adjacent to an ice shelf, it can follow deep bathymetric pathways into the neighbouring sub-ice shelf cavity and interact with the base of the ice to form Ice Shelf Water (ISW; Jenkins, 1991). These dense waters then accumulate on the continental shelf and migrate towards the shelf break to cascade down the continental slope as a gravity current (Gordon, 1986; Whitehead, 1987). As the waters descend towards the depths, they mix with and entrain ambient water masses until they reach either a density neutral depth, or the sea floor, at which point they spread outwards as Antarctic Bottom Water (AABW) (Bergamasco et al., 2003; Huthnance 1995). AABW plays a crucial role in the global overturning circulation, in abyssal ventilation and in the cross-basin transport of heat, salt, carbon, nutrients and numerous other tracers (Killworth, 1983; Johnson, 2008; Orsi, 2010). The principal locations for the formation of the source waters of AABW are the Weddell and Ross Seas adjacent to the large ice shelves (Orsi et al., 1999; van Caspel et al., 2015; Kerr et al., 2018; Bowen et al., 2021).

Filchner Ronne Ice Shelf (FRIS) is located at the southern boundary of the Weddell Sea and represents 28% of the total Antarctic ice shelf area (Fig. 1a). Traditionally FRIS has been viewed as having the greatest contribution to AABW by forming the coldest and most oxygen-rich dense waters in the Southern Ocean (Nicholls et al., 2009; Naveira Garabato et al., 2002). Observations for the southern Weddell Sea continental shelf indicate that HSSW enters the FRIS cavity following the Ronne Depression (Fig. 1a), circulates under the cavity causing melting at the base of the ice shelf at great water pressures and then exits as colder and fresher ISW via the Filchner Trough (Nicholls et al., 2001; Nicholls et al., 2004; Janout et al, 2021). This outflowing ISW mixes with HSSW formed on the shallow continental shelf adjacent to Berkner Island and cascades down the continental slope, mixing with ambient modified Circumpolar Deep Water (CDW) to form AABW (Fahrbach et al., 1995; Nicholls et al., 2009).

While the main formation site of the source waters of AABW in the Weddell Sea is the FRIS continental shelf, Larsen-C Ice Shelf (LCIS) is also thought to play an important role. Nestled into the arc of the Antarctic Peninsula (Fig. 1a), processes adjacent to this ice shelf produce a fresher variety of dense water called Weddell Sea Deep Water (WSDW), which is lighter than the Weddell Sea Bottom Water (WSBW) formed further south (Fahrbach et al., 1995; Gordon et al., 2001). This water mass is less hindered by bathymetric constraints so that it is more easily transported out of the gyre over the South Scotia Ridge to make an important contribution to AABW (Abrahamsen et al., 2019; van Caspel et al., 2015).

The Ross Sea, the second largest site for AABW formation, is home to Antarctica's largest ice shelf representing 32 % of the total Antarctic ice shelf area (Rignot et al., 2013). The Ross Ice Shelf (RIS) is located at the southern boundary of the Ross Sea (Fig. 1b) where the continental shelf has very irregular topography with numerous troughs and depressions that act as reservoirs for dense waters (Budillon et al., 2003). Just offshore, CDW flows largely un-modified within the Ross Gyre and mixes with the local waters at the shelf break (Fig. 1b), providing a source of heat and making this a region of dynamic water mass exchange (Bergamasco et al., 2003; Budillon et al., 2003). Two recurring ice-free zones are the principal formation sites for HSSW in the area: one located at the south-western corner of the Ross Sea called the Terra Nova Bay polynya and another in front of RIS called the Ross Sea Polynya. This HSSW then spreads both northwards towards the shelf break and

73 southwards under RIS (Fig. 1b). Similarly to FRIS, the HSSW flowing into the RIS cavity interacts with the base of the ice
74 shelf to form ISW (Jacobs et al., 1979).
75
76 While freshwater input to the ocean from ice shelf melt is (at present) relatively small in magnitude, it exerts a strong
77 modulating effect on dense water formation and Southern Ocean water mass transformation (Schodlok et al., 2015; Jeong et
78 al., 2020). The impacts of increased meltwater in a warming climate could, in addition to raising sea level, actually reduce
79 AABW formation with major consequences for global overturning (Silvano et al., 2018, Williams et al., 2016). One possible
80 series of events common to simulations by the E3SM, CSIRO Mk3L and LOVECLIM climate models describes how surface
81 freshening from ice shelf melt would increase stratification along the Antarctic coast, inhibit full depth convection and the
82 formation of dense shelf water, and simultaneously trap warm water at depth resulting in further ice shelf melting and a
83 horizontal propagation of the warming signal (Jeong et al., 2020; Phipps et al., 2016; Menviel et al., 2010).
84
85 Despite the importance of ocean-ice shelf interactions for the climate system, none of the models contributing to the DECK
86 experiments of the Coupled Model Intercomparison Project Phase 6 (CMIP6, used to inform the Intergovernmental Panel on
87 Climate Change (IPCC) assessment report 6 (AR6)) explicitly represented circulation within sub-ice shelf cavities (Heuze et
88 al., 2021). This has lowered confidence in projected trends for the Southern Ocean and has limited our ability to incorporate
89 the impacts of global ocean warming on the Antarctic Ice Sheet (Meredith et al., 2019; Beadling et al., 2020; Comeau et al.,
90 2022). In most coupled climate models, the formation of dense water is poorly represented as AABW is formed via open
91 ocean convection, often with mixed layers that are too deep, and polynyas that are too large and too frequent (Heuze et al.,
92 2013; Mohrmann et al., 2021). In reality, deep open-ocean convection events able to produce AABW are rarely observed
93 (Goosse et al. 2021) and instead ocean–sea-ice–atmosphere interactions adjacent to the Antarctic ice shelves are responsible
94 for the creation of the majority of AABW source waters.
95
96 The authors propose that the path towards improving AABW realism in coupled climate models starts with a more accurate
97 simulation of the dense precursors on the Antarctic continental shelf. Then, work needs to be done on improving the
98 overflows so as to facilitate the downslope export of these waters, and on decreasing the strength of open ocean convection
99 (Heuze et al., 2021). The Nucleus for European Modelling of the Ocean (NEMO) model is used as the ocean component in
100 many climate models (Hazeleger et al., 2010; Scoccimarro et al., 2011; Hewitt et al., 2011, 2016; Dufresne et al., 2013;
101 Voldoire et al., 2013; Cao et al., 2018; Swart et al., 2019) and consequently the development of configurations with
102 improved realism of Antarctic shelf water circulation and AABW source water properties is of interest to a large community.
103
104 Ice shelf melt has previously been represented using NEMO in a variety of ways: prescribed using a freshwater flux at the
105 surface, a fixed flux distributed over the depth range of the mouth of the ice shelf front, a specified melt at the base of the ice
106 shelf, and an interactive melt with both fixed geometry and evolving coupled ice shelves (Mathiot et al., 2017; Storkey et al.,
107 2018; Smith et al., 2021). The simulations with a fixed freshwater flux parameterization at depth perform well in terms of
108 mimicking the vertical overturning and associated entrainment of ice shelf melt, but do not allow for interactive ice-ocean
109 exchange that evolves with ocean properties. Parameterizations of ice shelf melt using far field temperature (outside of the
110 cavities) exist and an extensive comparison was undertaken in Burgard et al. (2022). Here they found that none of the
111 available parameterizations yield a negligible error, and so parameterizing basal melt still remains a challenge. Furthermore,
112 these parameterizations do not solve the need to allow for circulation underneath the ice shelves in order to produce the
113 horizontal variability observed on the continental shelf. For this, it is necessary to open the sub-ice shelf cavities in the
114 simulation (Mathiot et al., 2017; Storkey et al., 2018; Comeau et al., 2022). Of all the previous studies using NEMO
115 configurations with explicit sub-ice shelf cavities, only one has been at a resolution that is compatible with long-term climate
116 projection applications, that developed by Smith et al. (2021) where a global ocean 1° NEMO (eORCA1) is coupled with

interactive ice sheets in the the U.K. Earth System model (UKESM). Previous studies have proven very useful in illustrating the strengths and weaknesses of NEMO's representation of ocean-ice shelf interactions but the results apply to regional configurations (e.g. Mathiot et al., 2017; Jourdain et al., 2017; Hausmann et al., 2020; Huot et al. 2021) or high resolution global configurations (e.g. 1/4° and 1/12° in Storkey et al., 2018) and so do not fit the needs of typical CMIP models. The results presented by Smith et al. (2021) for UKESM with NEMO eORCA1 coupled to an Antarctic ice sheet model highlight the substantial advancement in model development, but do not show how this coupling affects the realism of Southern Ocean water mass properties and dynamics. Evaluation of the initial state of the UKESM (NEMO coupled to BICYCLES ice sheet model) was undertaken by Siahaan et al. (2021), but the investigation served to check for the absence of large biases and so an in-depth comparison was not carried out.

A gap therefore exists to take a step-by-step approach to represent ice shelf-ocean interactions in NEMO for climate applications. Additionally, a well documented description of one possible method to simulate sub-ice shelf cavity circulation in low resolution ocean models could be of use in the designing of the next phase of CMIP. In this study we present the first proposed step in this journey by explicitly simulating circulation under only RIS, FRIS and LCIS. These ice shelves were chosen due to their direct role in the formation of the parent waters of AABW (Kerr et al., 2018; Bowen et al., 2021), and due to their large size and thus practicality of realistically simulating their sub-ice shelf cavities in a global ocean 1° setup. We choose to keep all other ice shelf cavities closed with prescribed melt rates injected at the mouth of the front using the method described by Mathiot et al. (2017). This includes the relatively large Amery Ice Shelf cavity, despite its role in preconditioning bottom water formation in the Cape Darnley polynya (Williams et al., 2016), because this polynya is absent in our configuration (due to the absence of icebergs and landfast sea ice). We choose to explore the changes in circulation, melt rates, and water mass properties in the Weddell and Ross Seas in a forced scenario with fixed cavity geometry, as coupling can introduce further biases and obscure the changes attributed to sub-ice shelf circulation. By taking this circumspect approach it is possible to diagnose the impact of ocean-ice shelf interactions on the parent waters of AABW and produce a validated configuration of NEMO that can either be used for the next generation of climate models or as an interim step towards dynamic ice-sheet coupling.

The model setup, configurations used in this study, forcing, and methodology to establish initial conditions under the ice shelves are described in Sect. 2. A validation of the reference configuration compared to ocean observations is presented in Sect. 3. Sect. 4 then explores the results from the "Open" cavity simulation and compares melt rates and thermohaline properties with other model estimates and observed values. Sect. 5 provides the reader with a summary discussion, and Sect. 6 presents a conclusion of the findings of this study. Additional information regarding model namelist nomenclature, representation of tides, an investigation into sea ice production, and plots showing AABW volume and bottom density changes are provided in Supplementary Material.
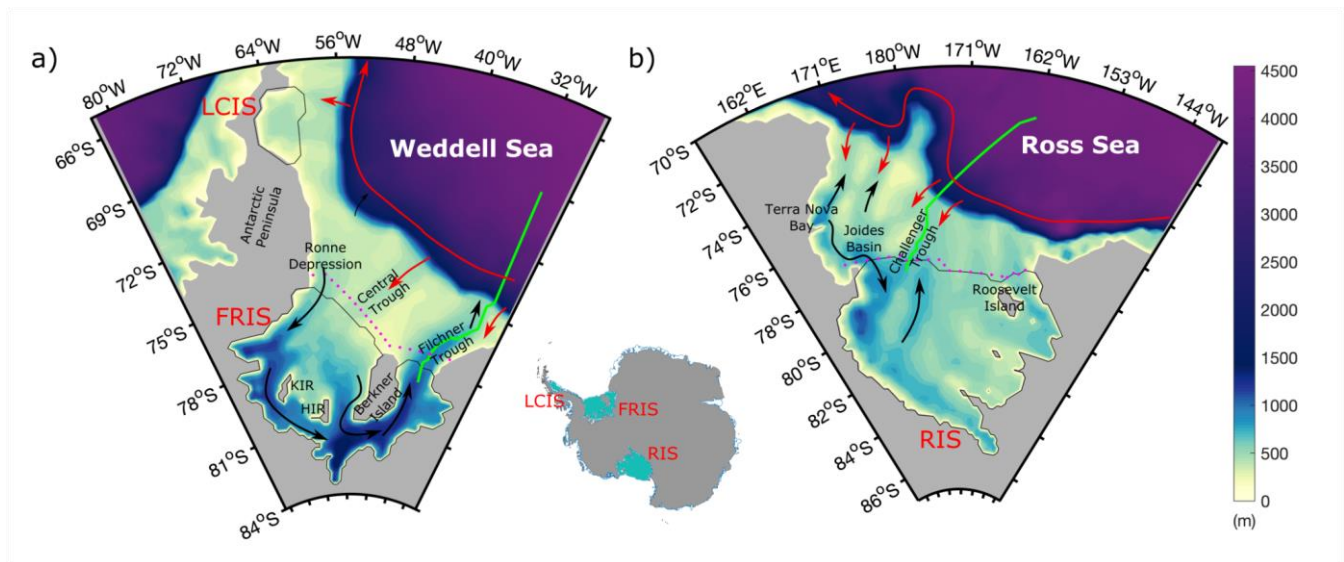
151

152 Figure 1: Model bathymetry for (a) the Weddell and (b) Ross Seas with main topographic features labeled (KIR: Korff Ice
153 Rise; HIR: Henry Ice Rise). Red arrows show direction of flow of warm deep water and black arrows indicate dense shelf
154 water circulation according to observational estimates. Circulation features depicted in this figure are adapted from
155 information presented in Budillon et al. (2003), Bergamasco et al. (2003), Russo et al. (2011) and Janout et al. (2018).
156 Magenta dotted lines indicate sections used for CTD comparisons and green lines show shelf cross sections used for analysis
157 in Figs. 6 and 7.

158 **2 Methods**

159 **2.1 Model setup**

160 For this study, we use version 4.2 of NEMO (NEMO System Team, 2022). NEMO is a three-dimensional, free-surface,
161 hydrostatic, primitive-equation global ocean general circulation model. Our configuration uses the eORCA1 global grid with
162 nominal horizontal resolution of 1° at the equator and a reduction in meridional grid spacing towards higher latitudes to
163 match the accompanying shrinking of the zonal dimension of the grid cells. In the Southern Hemisphere, the model grid has
164 been extended to reach 85° S to allow for the representation of the sub-ice shelf seas according to the procedure described in
165 Mathiot et al. (2017). The average horizontal resolution of the grid under RIS, FRIS, and LCIS is 20 km, 22 km and 42 km
166 respectively. To account for the decrease in the horizontal size of grid cells at high latitudes, we decide to linearly scale the
167 laplacian eddy viscosity south of 65° S according to grid cell size. In the vertical, the configuration possesses 75 levels, with
168 thickness increasing from 1 m at the surface to 200 m at depth (Storkey et al., 2017). We use the z* vertical coordinate
169 adapted to the ice shelf so that all cells between the surface and the ice shelf base are masked at initialisation and the effect
170 of the ice shelf on friction and pressure gradient is calculated (Madec and NEMO System Team, 2019; Mathiot et al., 2017).
171 The bathymetry used is derived from the Earth TOPOgraphy version 2 data set (ETOPO2v2; NOAA, 2006) with information
172 for the extension under the ice shelves based on the International Bathymetric Chart of the Southern Ocean (IBSCO; Arndt
173 et al., 2013). For the calculation of the thermodynamic properties of seawater, NEMO uses the Thermodynamic Equation Of
174 Seawater - 2010 (TEOS-10) giving results in conservative temperature and absolute salinity, which for the purposes of this
175 study, were converted to potential temperature and practical salinity in order to facilitate comparison of the model results

with observations and known signatures of water masses. For more information regarding the choices of advection and diffusion schemes, mixing coefficients, and eddy parameterizations, please refer to the copy of the namelists provided in the accompanying data repository. A note explaining the nomenclature of the namelists and the differences between the "Open" and "Closed" cavity simulations can be found in Supplementary Material Sect. S1.

The effect of tides on vertical mixing (through breaking of internal waves) is taken into account in NEMO using the energy constrained parameterization of de Lavergne et al. (2020). This mixing parameterization does not, however, represent trapped waves at high latitudes or any tide-induced internal-wave mixing below ice shelves, and does not include the effect of tides on basal friction and thus melting of the ice shelves. To address this, by default there is a parameter (rn_ke0) representing the background kinetic energy associated with tides which is set to a constant of 2.5×10^{-3} m^2 s^{-2} everywhere. We tested another methodology of parameterizing the impact of tides on melting according to Jourdain et al. (2019) using CATS2008 two-dimensional tidal velocities; as summarised in Supplementary Material Sect. S2 and Fig. S1, this alternative parameterization brings marginal changes in the simulated melt patterns and bulk melt rates (< 10 %). The explicit representation of tides is not advisable in a configuration designed for climate applications due to the high levels of numerical mixing induced.

The ocean dynamics component, NEMO OCE, is coupled with SI^3, the dynamic and thermodynamic sea ice model of NEMO (Rousset et al., 2015; Vancoppenolle et al., 2023). SI^3 is directly resolved on the ocean grid, based on an energy- and salt- conserving approach for sea ice thermodynamics (Vancoppenolle et al., 2023), multiple categories to resolve subgrid scale variations in ice thickness (Bitz et al., 2001; Lipscomb, 2001), a second-order moment-conserving scheme for horizontal advection (Prather, 1986), and the adaptive elastic-viscous-plastic formulation for the rheology term of the momentum equation (Kimmritz et al., 2016).

2.2 Open vs Closed Configurations

Here, we present results from two configurations: first a "Closed" cavity reference configuration where ice shelf melt is prescribed in a way that mimics the ice-shelf overturning, and secondly an "Open" cavity configuration. For the reference "Closed" cavity configuration, a fixed freshwater flux corresponding to the volume of basal meltwater estimated by Depoorter et al. (2013) for each ice shelf is added into the ocean evenly between the ocean floor and the base of the ice shelf, horizontally uniform across the ice shelf front, and a vertical wall closes the cavity at this location (as in Mathiot et al., 2017). The fixed freshwater flux is based on Depoorter et al. (2013) melt estimates as this is the same file used for the IPSL climate model. Furthermore, the ice shelf area surveyed by Adusumilli et al. (2020) only extends to 81.5 °S so that RIS and FRIS are not fully covered and therefore don't have the full melt flux. For the "Open" cavity configuration, the majority of ice shelves are kept closed using the same method as described above and only three of the largest cold water ice shelves are opened. Circulation is simulated under RIS, FRIS and LCIS where the prescribed freshwater flux is turned off at the mouths of these cavities and interactive melt is activated. Ice shelf melt and freeze are calculated using the 3-equation formulation (Hellmer and Olbers, 1989; Holland and Jenkins, 1999; Asay-Davis et al., 2016) in which the temperature, salinity and velocities are averaged over a fixed boundary layer thickness of 30 m chosen according to Losch (2008). The top drag coefficient used is 10^{-3} and the temperature and salinity transfer coefficients used are 1.4×10^{-2} and 4×10^{-4} respectively. Note that a fixed ice shelf geometry is maintained, thereby assuming a steady-state where all ice melted by the ocean is replaced by the seaward advection of new ice (Schodlok et al., 2015; Mathiot et al., 2017).

By using this combination of explicit and parameterized ice shelf cavities, we provide an intermediate step between prescribed melt and explicit cavities or even ice sheet coupling, and gain experience and a better understanding of the impact

on ocean dynamics in order to better inform future choices. The advantage of this approach is that it allows us to specify the melt for small cavities which remain unresolved or insufficiently resolved at a 1° resolution, and simultaneously utilize the model capability to resolve sub-ice shelf cavity circulation under the large cold ice shelves, which allows for more realistic formation of the source waters of AABW. In terms of computing cost, the "Open" cavity configuration costs 11% more than the "Closed" cavity simulation (mostly due to addition of cells as the model grid is extended further south; only 0.3% of this is associated with the cost of the ice shelf routines themselves). Figure 1 shows the extended bathymetry of eORCA1 for the Weddell and Ross seas with the three ice shelf cavities of interest un-masked and important features labelled.

2.3 Forcing

For both "Open" and "Closed" configurations, the model was run for 124 years using 2 cycles of interannual (1948-2009) CORE forcing (Coordinated Ocean - ice Reference Experiments version 2; Large & Yeager, 2004; Griffies et al., 2009). Sea surface salinity restoring is activated, but not under sea ice as we have low confidence in the sea surface salinity climatology in this area due to limited observations. Freshwater discharge from iceberg melt is parameterized using a prescribed surface flux with realistic distribution (Merino et al., 2016), based on calving estimates from Depoorter et al. (2013).

2.4 Initial conditions

For all simulations, global ocean properties were initialized using the 1981-2010 climatology of World Ocean Atlas 2013 (WOA2013; Locarnini et al., 2013; Zweng et al., 2013) as this dataset is used for the IPSL climate model and so was a convenient choice. This climatology does not, however, extend under the Antarctic ice shelves and so in order to provide somewhat realistic initial conditions underneath FRIS, LCIS, and RIS, we employed an idealized regional configuration of each ice shelf. For this we created a NEMO test case using a closed domain, with temperature and salinity restoring at the boundaries, 75 vertical layers and a resolution, timestep and bathymetry corresponding to that of eORCA1. The domain for each of the 3 configurations included just the ice shelf and adjacent continental shelf and slope and so were reasonably low-cost and fast to run in order to perform sensitivity experiments. The simulations were initialized with a constant and uniform temperature and salinity and restored at the boundaries using a mean profile from WOA2013 for that region. The choices for initial thermohaline properties inside the cavities were informed by calculating the mean values of detected ISW from CTD observations performed in the area adjacent to each ice shelf and converting these to conservative temperature and absolute salinity for input to the model [-2 °C and 34.76 for FRIS (Janout et al., 2021), -1.95 °C and 34.74 for LCIS (Nicholls et al., 2004; Hutchinson et al., 2020), and -1.94 °C and 34.76 for RIS (Bergamasco et al., 2003; Budillon et al., 2003)]. Each simulation was run for 10 years, which was found to be sufficiently long to spin-up the circulation within each cavity and reach a stable melt rate. The temperature-salinity distributions within the cavity were extracted and merged with WOA2013 data re-gridded to the NEMO eORCA1 grid, with a cubic spline used to smooth the data discontinuity across the ice shelf front. By following this method we have attempted to provide as realistic initial conditions for eORCA1 as possible with the simulation starting with CORE forcing from the 1st of January 1948.

3 Water mass realism in NEMO without cavities

To assess the existing biases in the representation of dense water properties in NEMO v4.2 eORCA1 standard configuration ("Closed"), full depth temperature versus salinity plots along with bottom temperature and salinity are compared with World Ocean Atlas (WOA 2018) gridded observations from 1981-2010 (Locarnini et al., 2018; Zweng et al., 2019) in Figs. 2 and 3 for the Weddell and Ross Seas, respectively.

264   WOA observations indicate the presence of HSSW on the south-western continental shelf of the Weddell Sea, possessing
265   salinities of up to 34.9 psu, likely sourced from the coastal polynya along the western flank of FRIS ice shelf front
266   (Supplementary Material Fig. S2a). On the eastern side of the FRIS ice shelf front, evidence of ISW can be seen with
267   temperatures below surface freezing point (-1.9 °C) and fresher salinities of around 34.65 psu (Figs. 2b and 2c). Results from
268   CTD observations obtained on the continental shelf in front of FRIS propose a counter-clockwise circulation pattern with
269   HSSW entering the cavity via the Ronne Depression and ISW exiting via the Filchner Trough (Fig. 1a; Janout et al., 2021).
270   By comparison, the standard model configuration is overall too salty on the continental shelf with HSSW properties that are
271   out of the bounds of the observed range (HSSW box Fig. 2d). Most notably, there is a pool of HSSW that has built up in the
272   Ronne Depression resulting in overestimations of bottom salinity and exaggerated cool conditions on the southwestern
273   Weddell shelf (Figs. 2e and 2f). In terms of ISW, there is none detected in the model output (ISW box Fig. 2d), as in this
274   configuration there is no explicit ocean-ice shelf interaction. Offshore bottom temperature is overall colder than in WOA,
275   resulting in a core AABW signature that is at the lower limit of observed values (Fig. 2d). This is indicative of the effects of
276   strong open ocean deep convection (Heuze et al., 2021) which is discussed further in Sect. 4.4.
277
278   Due to the limited observations adjacent to LCIS, WOA bottom properties do not capture the cold water masses located on
279   the continental shelf detected by Hutchinson et al. (2020), where bottom temperatures of below -2 °C and salinities of 34.6
280   psu were reported. Instead Fig. 2b indicates very warm conditions (temperatures of around 0.5°C) on the western flank of the
281   Weddell Sea. The authors explored the bottom properties in this area in the Southern Ocean State Estimate (SOSE; Mazloff
282   et al., 2010) atlas and found bottom temperatures on the shelf adjacent to LCIS in line with those reported from hydrographic
283   observations (-2 °C) but the bottom salinities were found to be far too fresh (34.5 psu). A fair comparison can therefore not
284   be realistically made between NEMO and an atlas for the area adjacent to LCIS, but by comparing the model output with the
285   CTD results from Hutchinson et al. (2020; their Fig. 3b), we find the "Closed" configuration to be too saline with bottom
286   salinities (34.8 psu) greater than that observed. The overly saline conditions along the western flank of the Weddell Sea are
287   likely a spill-over effect from the HSSW buildup seen in the Ronne Depression further south (Fig. 2f).
288
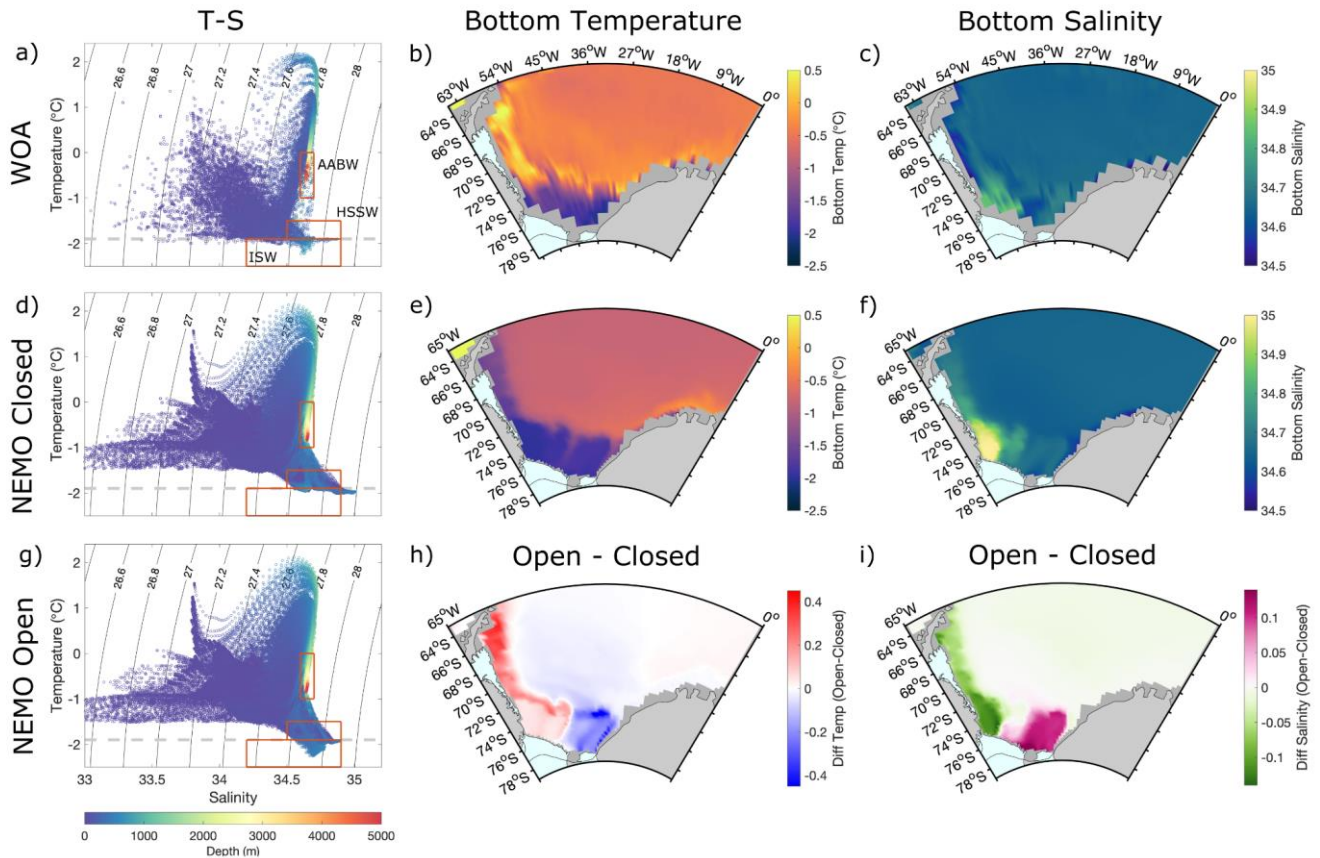
Figure 2: Weddell Sea comparison of NEMO v4.2 eORCA1 reference configuration ("Closed"; subplots d-f) for equivalent years 1981-2009 to be compared with World Ocean Atlas (WOA; Locarnini et al., 2018; Zweng et al., 2019) observational dataset (subplots a-c). The temperature salinity-distributions in density space are shown in plots (a), (d) and (g) with the dashed gray line representing surface freezing point and labels in plot (a) indicating the observed ranges for properties corresponding to Antarctic Bottom Water (AABW), High Salinity Shelf Water (HSSW) and Ice Shelf Water (ISW) (Robertson et al., 2002; Hutchinson et al., 2020). Plots (b), (c), (e) and (f) show bottom temperature and salinity of WOA and "Closed", and the difference in bottom properties between the "Open" and "Closed" cavity configurations (Open - Closed) are shown in subplots (h) and (i). Panels (a) and (g) exclude ice shelf cavity data matching the "Closed" configuration of panel (d).

WOA bottom temperatures and salinities for the Ross Sea indicate a strong east-west gradient in properties across the continental shelf (Figs. 3b and 3c). Conditions in the south west reveal the cold and salty signature of HSSW likely formed in the Terra Nova Bay polynya and the Ross Polynya. Intrusions of CDW at the eastern portion of the RIS front can be seen by warm signatures of up to 1 °C (Fig. 3b) and fresher bottom salinities (Fig. 3c). Hydrological and current meter data presented by Budillon et al. (2003) reported that HSSW dominates bottom properties within the troughs connected to the Joides Basin, and ISW dominates in the Challenger Trough (see locations of bathymetric features in Fig. 1b), thus indicating a western intensified anticlockwise circulation cell under RIS. In terms of HSSW properties, the model is within the observed range (Fig. 3d), yet the proportion and salinity of HSSW in Terra Nova Bay and Joides Basin appear to be

309 overestimated (Fig. 3f). The bottom temperatures from NEMO indicate the presence of very warm waters, likely of
310 circumpolar origin right on the eastern continental shelf (Fig. 3e) whereas in observations this shelf is found to be cold and
311 the warm water confined offshore of the shelf break with only occasional intrusions (Bergamasco et al., 2003; Fig. 3b).
312 Again, there is no ISW in this standard configuration, as there is no explicit model representation of ice shelf-ocean
313 interactions. Offshore bottom properties are slightly cooler than WOA in the model, but the AABW signature (AABW box
314 Fig. 3d) falls within the range reported from observations (Bergamasco et al., 2002; Bouillon et al., 2011; Silvano et al.,
315 2016).
316
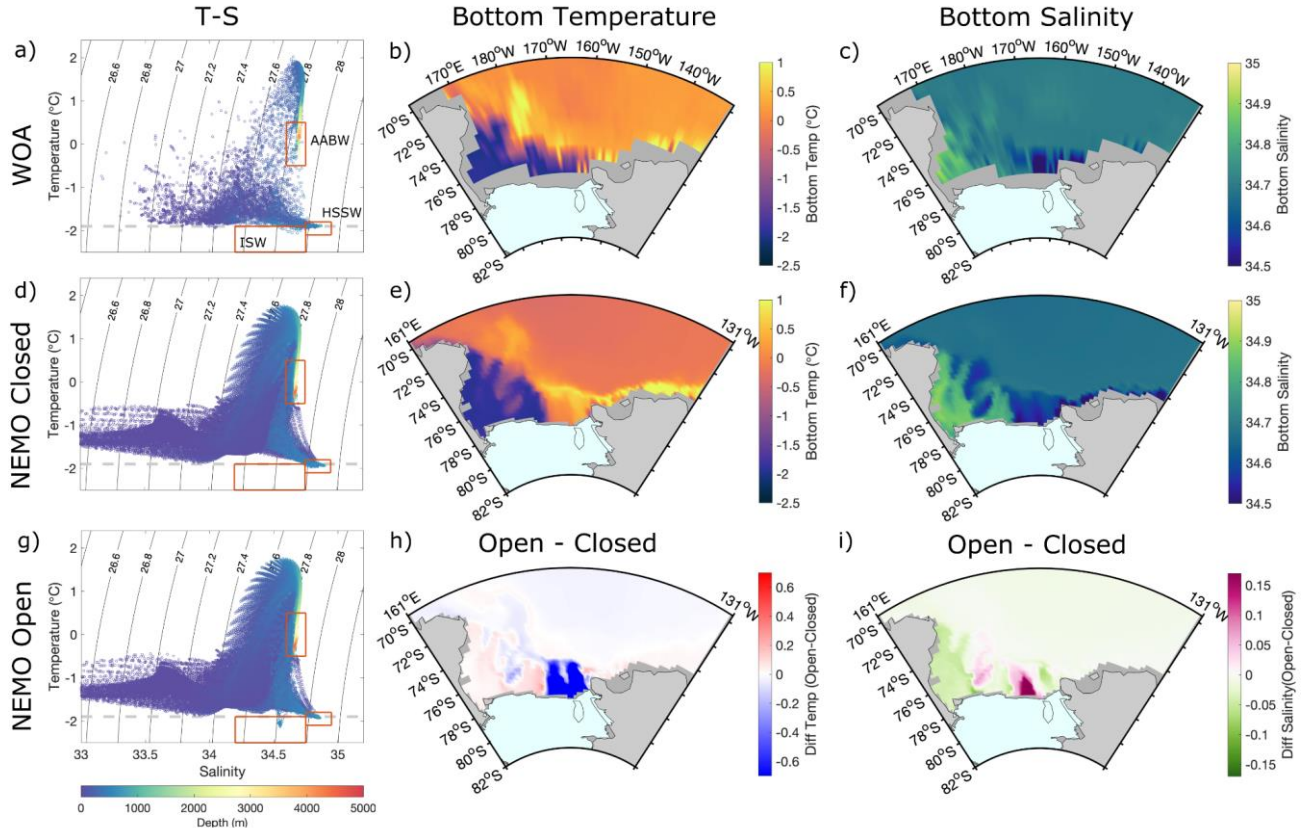
317
318
319 Figure 3: Same as Fig. 2 but for the Ross Sea.
320
321
322 **4 Impact of explicit sub-ice shelf circulation**
323
324 The following sections present results pertaining to the "Open" cavity run where the eORCA1 grid is extended under FRIS,
325 LCIS and RIS to allow for circulation within the cavities and explicit interaction with the base of these ice shelves.
326
327 **4.1 Melt rates**
328

The average ice shelf melt rate pattern for FRIS, LCIS and RIS is shown in Fig. 4 for the model simulation equivalent years 1995 to 2009, where orange indicates melt and purple shows refreezing. The average total melt flux for this time period is shown in Table 1 and compared to Depoorter et al. (2013) from which the volumes for the prescribed melt were taken for the reference configuration ("Closed"). Opening the cavities results in at least double the melt reported from Depoorter et al. (2013). This discrepancy reflects both a warm bias on the continental shelf in NEMO (Sect. 4.4) and a possible bias in Depoorter's estimates which are lower than all other satellite estimates (Table 1). The total melt fluxes of each ice shelf from various other observational and model studies are also listed in the table showing the wide spread in basal melt estimates both within values calculated from observations and between observations and models (Table 1). The model studies of Mathiot et al. (2017) and Bull et al. (2021), which are both regional NEMO 1/4° configurations, and the NEMO 1/12° configuration of the southwestern Weddell Sea of Haussmann et al. (2020), are particularly relevant to compare eORCA1 with, as here we see the possible impact of lowering the resolution in NEMO. For the Weddell Sea, our global 1° (eORCA1) compares well with these regional high resolution studies producing a net basal melt within 12 Gt/yr of the other estimates for FRIS and LCIS. The eORCA1 melt rate for RIS, while higher than observational studies, is in the middle of other model estimates, and is especially well aligned with that of NEMO 1/4° from Mathiot et al. (2017). Overall, eORCA1's total melt fluxes correspond well with the average from all other estimates and are well within the standard deviations (last line of Table 1).

	Values in Gt/yr	FRIS	LCIS	RIS
	NEMO 4.2 eORCA1 (1995-2009)	117 ± 21	36 ± 7	112 ± 22
Obs	**Depoorter et al., 2013** (1995-2009)	50 ± 40	18 ± 8	34 ± 25
	Adusumilli et al., 2020 (1994-2018)	81 ± 123	78 ± 99	80 ± 82
	Rignot et al., 2013 (2003-2008)	155 ± 36	21 ± 67	48 ± 24
	Moholdt et al., 2014 (2003-2009)	124		50
Models	**Mathiot et al., 2017** (1988)	123	46	111
	Timmermann et al., 2012 (1980-1999)	138	48	260
	Hellmer et al., 2004 (1978-1997)	119	38	180
	Naughten et al., 2018 (FESOM HR) (2002-2016)	115	55	112
	Naughten et al., 2018 (MetROMS) (2002-2016)	46	18	54
	Haussmann et al., 2020 (1993-1997)	105	24	
	Bull et al., 2021 (1986-2017)	124		
	Average from all the above excluding present study	111 ± 33	37 ± 21	118 ± 87

Table 1: Comparison of mean total melt flux (Gigatons per year) for Filchner-Ronne (FRIS), Larsen C (LCIS) and Ross Ice Shelves (RIS) for observational and model studies. The mean and standard deviation of all the estimates depicted in the table excluding the current study are shown at the bottom.

351   The patterns of melt shown in Fig. 4 also compare well with those of observational estimates like Rignot et al. (2013; their
352   Figure 1) and high resolution model results like Haussmann et al. (2020; their Figure 3) whose color bar we replicated for
353   ease of cross-comparison. If we look at the melt pattern of FRIS and compare it with these two aforementioned studies, we
354   see that eORCA1 captures the high melt rates at the western portion of the ice shelf front, at the southern edge of Berkner
355   Island and along the grounding line at the back of the cavity. The model also correctly simulates the region of refreezing
356   along the western boundary of the circulation cell within the cavity, in both the Ronne and Filchner depressions and the re-
357   freezing in the shallow region between the Korff and Henry Ice Rises (Fig. 4a, see bathymetry location in Fig. 1a). For LCIS,
358   the entire shelf shows a positive melt (Fig. 4b). Observations from Rignot et al. (2013) and simulations from Harrison et al.
359   (2022) indicate some re-freezing under this ice shelf but the regional high resolution model studies of Mathiot et al. (2017)
360   and Haussmann et al. (2020) similarly show melting only. The pattern for RIS generally compares well with that reported
361   from observations but the magnitude of melt at the ice shelf front, especially to the east, is elevated (Fig. 4c).
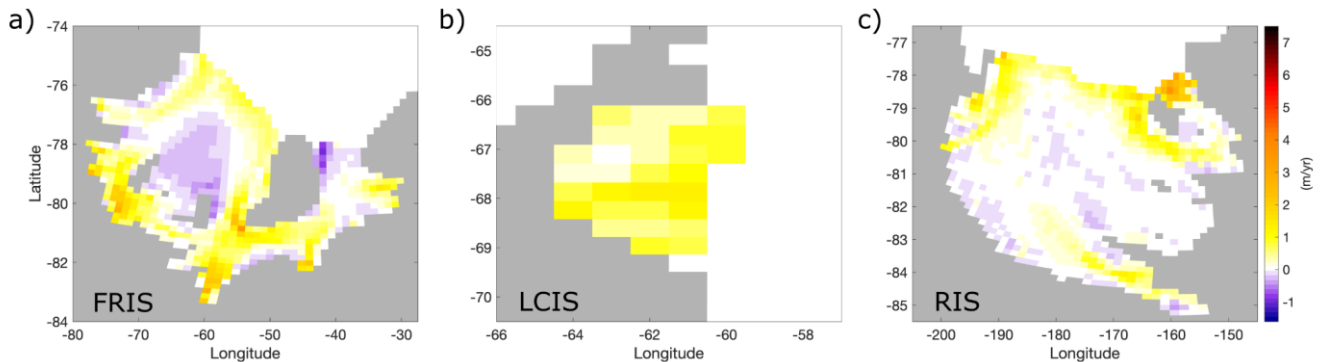
362
363   Figure 4: Melt rates in meters per year for (a) Filchner-Ronne Ice Shelf, (b) Larsen C Ice Shelf and (c) Ross Ice Shelf where
364   orange indicates melt and purple re-freezing. The results are mean values for the model equivalent period 1995-2009.
365
366
367   **4.2 Circulation and properties**
368
369   Opening the sub-ice shelf cavities in eORCA1 allows for the establishment of a horizontal gyre circulation within the cavity
370   and on the continental shelf of the Weddell and Ross Seas, in line with previous studies (Losch et al., 2008; Mathiot et al.,
371   2017).
372
373   The mean state of circulation from the last 10 years of simulation within the FRIS cavity, along with the associated bottom
374   thermohaline properties can be seen in Figs. 5a-5d. The circulation patterns shown here are in good agreement with Bull et
375   al. (2021) at 1/4° and with Hausmann et al. (2020) at 1/12° with the exception of higher bottom salinities in eORCA1 and a
376   slightly weaker barotropic circulation strength. Note that here we use potential temperature and practical salinity so as to be
377   in line with the other figures of this paper, so approximately 0.17 psu must be added when juxtaposing with absolute salinity
378   plots. The depth averaged velocity and barotropic circulation pattern in Figs. 5a and 5b both indicate an anticlockwise
379   circulation under the ice shelf. Comparatively warm and salty HSSW enters via the Ronne Depression, circulates from west
380   to east, melts the base of the ice shelf mostly along the grounding line (cold, fresh signatures in Figs. 5c and 5d), and exits
381   via the Filchner Trough as ISW. This pattern is consistent with observations (Nicholls et al., 2001; Janout et al., 2021). Two
382   pathways of Modified Circumpolar Deep Water (MCDW) towards the ice shelf front can be seen, both in the circulation
383   pattern (Fig. 5a) and via the bottom temperature (Fig. 5c): one located in the middle of the continental shelf (Central Trough)

384 and the other on the shelf to the east of Filchner Trough. These pathways provide a conduit for heat towards the ice shelf and
385 facilitate the mixing of shelf water masses with MCDW. It is therefore encouraging that eORCA1 (with an effective
386 horizontal resolution under FRIS of 22 km) captures these, as they could play an important role in the evolution of shelf
387 circulation in future climate scenarios (Naughten et al., 2021).
388
389 Moving now to the Ross Sea, the time mean circulation pattern under RIS along with the bottom temperature and salinity
390 can be seen in Figs. 5e-5h. Here, we notice a strong anticlockwise circulation concentrated at the western boundary with
391 reduced magnitude currents towards the back and east of the cavity. The west of the cavity is overall warmer and saltier and
392 the east shows signatures of ISW. Bottom temperature indicates the presence of a cold ISW plume exiting the cavity to the
393 far east (Fig. 5g), which is not seen in the time averaged velocities or barotropic streamfunction, likely because the
394 associated speeds are slow. Instead, the simulated circulation indicates an offshore advection of sub-ice shelf water following
395 the Challenger Trough (see location marked in Fig. 1b). This water mass is likely recirculated HSSW as its temperature
396 remains at surface freezing point (-1.9 °C). A strong clockwise circulation cell offshore of RIS (red in Fig. 5f) brings warm
397 CDW into contact with the ice shelf front to the east, mixing out the signature of ISW further offshore (Fig. 5g). While this
398 simulated circulation pattern agrees well with that described by observations (Fig. 1; Bergamasco et al., 2003; Budillon et
399 al., 2003), it is likely too strong, resulting in an exaggerated net melt flux compared to the observational estimates (Table 1;
400 anomalously high melt at the eastern portion of the ice shelf front in Fig. 4c).

401
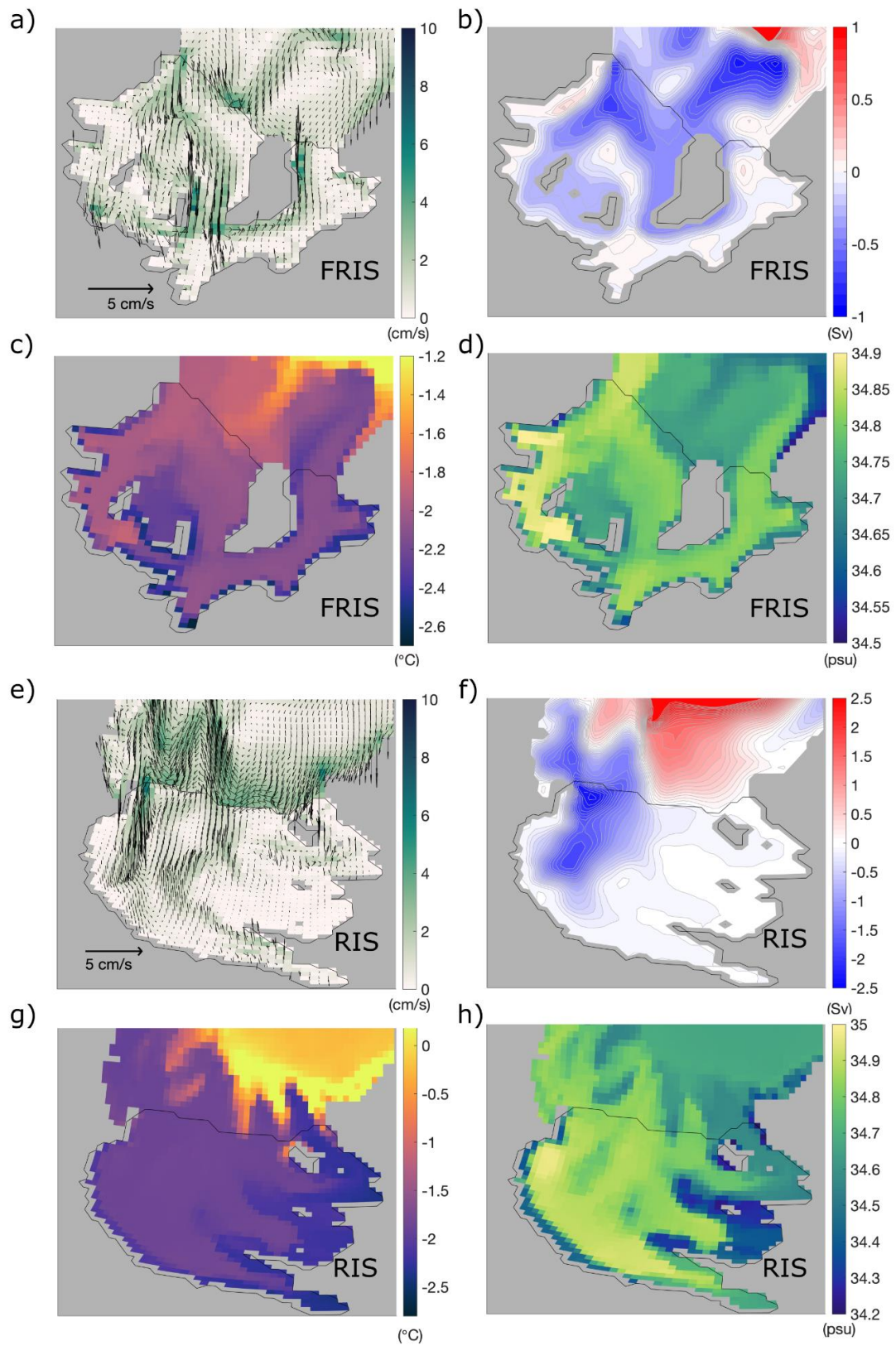
Figure 5: Circulation pattern and characteristics of properties under Filchner Ronne (a-d) and Ross (e-h) ice shelves for the last 10 years of the open cavity experiment. Subplots (a) and (e) show depth averaged velocity, (b) and (f) barotropic stream function, (c) and (g) bottom potential temperature and (d) and (h) bottom practical salinity (as opposed to conservative and absolute shown in Bull et al., 2021).

4.3 Impact on offshore properties

To highlight the impact of opening the FRIS, LCIS and RIS sub-ice shelf cavities on the offshore properties, Figs. 2g and 3g show the temperature versus salinity distribution excluding the data under the ice shelves. The differences in bottom temperature and salinity can be seen in Figs. 2h and 2i for the Weddell Sea and 3h and 3i for the Ross Sea.

A significant improvement in the representation of Weddell shelf water properties is evident as now HSSW is within the observed range and ISW is detected on the continental shelf (see HSSW and ISW red boxes in Fig. 2g). Opening the sub-ice-shelf cavity of FRIS has allowed the HSSW that previously built up in the Ronne Depression to advect under the ice shelf, become modified through basal interactions and exit the cavity as colder and fresher ISW. Consequently, the temperature and salinity differences are polarized west and east with warmer fresher conditions along the entire western boundary of the Weddell Gyre and cooler saltier conditions on the eastern continental shelf (Figs. 2h and 2i). These results agree well with those of Mathiot et al. (2017). The impact of opening LCIS can be seen via the maintenance of cold bottom properties immediately to the north (despite the fact that the shelf circulation has changed so that HSSW no-longer floods this region), along with the presence of a large negative salinity anomaly indicative of ice shelf melt (Fig. 2i). As the simulation is only 124 years long, the impact of opening the cavities on AABW cannot be fully assessed due to the slow renewal of this water mass at the bottom of the global ocean. A small change in signature of AABW can, however, be seen in the volumetric T-S plot (Supplementary Material Fig. S3a), where explicit ocean-ice shelf interaction results in a shift in volume towards cooler, fresher AABW (Open - Closed weighted average shift in AABW volume by -0.008 °C and -0.003 psu). This shift is accompanied by a small increase in volume of the water mass by 0.23 % (AABW limits delineated in green in Fig. S3a).

The impact of opening the RIS cavity on offshore properties can be seen in Figs. 3h and 3i. Similar to the Weddell Sea, conditions in the west, where in the reference run HSSW was built up, now become warmer and fresher as the path under the ice shelf is open. The signature of the cold plumes of dense shelf water (Fig. 5g) on either side of Roosevelt Island can clearly be seen in the temperature difference plot (Fig. 3h), but curiously they do not possess the same salinity anomaly (Fig. 3i). The positive salinity difference of the western plume indicates that this water is a variety of HSSW which has circulated under the ice shelf and was previously not present in this area. The small negative anomaly to the east indicates that this cold plume is, as previously hypothesised, outflowing ISW. Small temperature differences on the continental slope and further offshore indicate that there has been some communication of the changes in shelf waters further afield. The volumetric T-S plot for the Ross Sea found in Supplementary Material (Fig. S3b) indicates that opening the RIS cavity has moved the core of AABW towards slightly cooler fresher values, accompanied by a 0.34 % decrease in volume of AABW as defined by the original water mass limits (delineated in green in Fig. S3b; Open - Closed weighted average shift in AABW volume by -0.001 °C and -0.005 psu).

4.4 Comparison with ice shelf front CTD observations

The differences in circulation patterns and in thermohaline properties that result from opening the RIS and FRIS cavities documented above do not elucidate whether or not we have reduced biases and improved the realism of shelf waters in

446   eORCA1. For this, a direct comparison with in-situ observations is necessary. Due to the remote location of these ice shelves
447   and the harsh conditions associated with obtaining hydrographic samples in these areas, there are limited observations, and
448   so optimally interpolated atlases such as WOA or ocean reanalysis products like SOSE miss important local features or
449   seasonal variability. For comparison purposes, we have consequently selected CTD data from research cruises that have
450   sampled transects across the front of the ice shelves and extracted the model data corresponding to the approximate ship's
451   track using PAGO, a tool to analyze gridded ocean datasets (Deshayes et al., 2014).
452
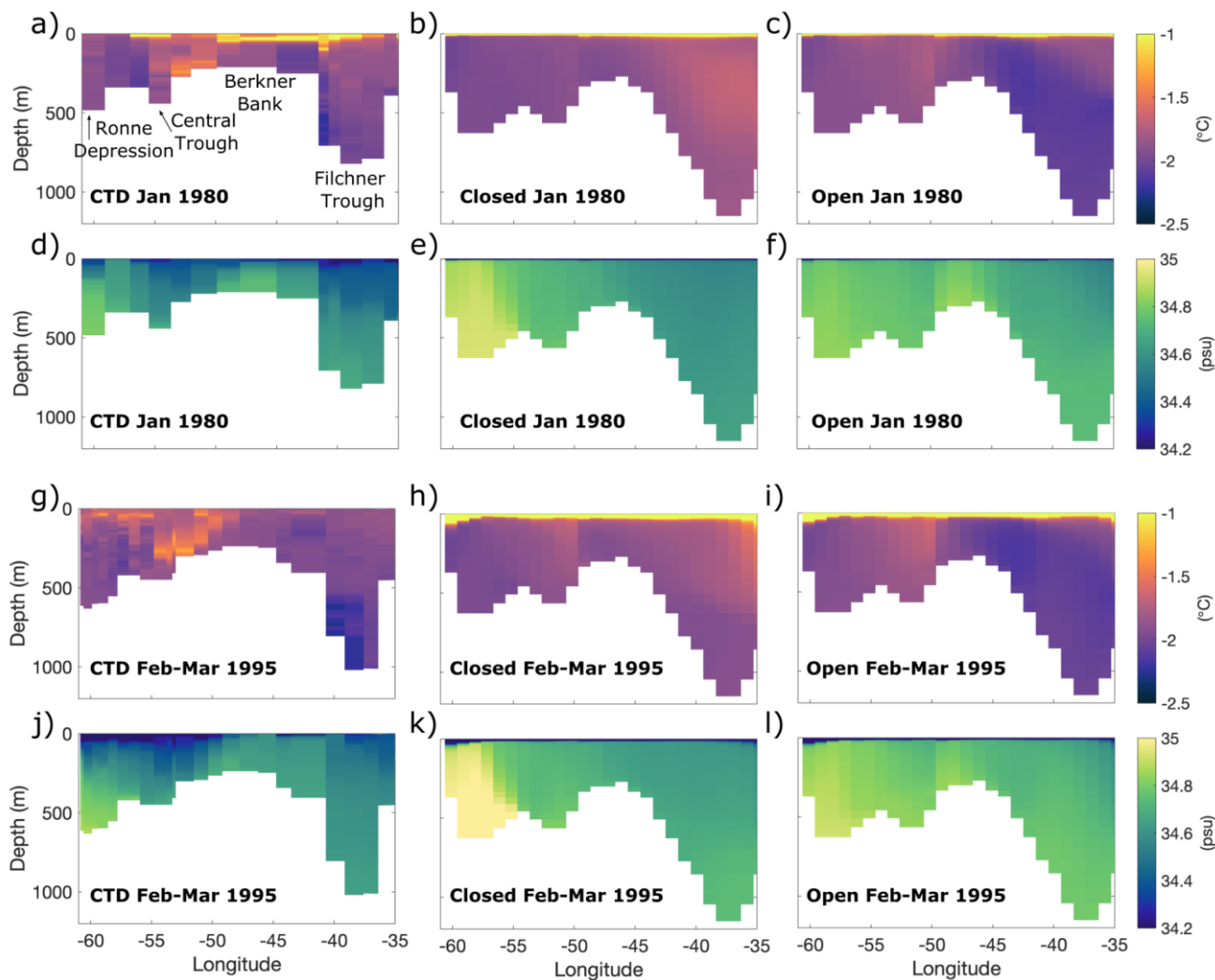
453
454
455   Figure 6: Validation of properties across the Filchner Ronne Ice Shelf front by comparing closed and open cavity NEMO
456   results with measured values from CTD sections performed in 1980 (Rohardt et al., 2016) and 1995 (Janout et al., 2021).
457   The model output for the corresponding equivalent year and month was extracted for more accurate comparison.
458   Bathymetric features discussed in the text are labelled in subplot (a).
459

460 For FRIS we use two CTD sections across the ice shelf front undertaken in 1980 and 1995 on board the RV Polarstern by the
461 Alfred Wegener Institute (Rohardt et al., 2016; Janout et al., 2021). The location of the section selected in NEMO to
462 approximately overlay the CTD transects can be seen as a magenta dotted line in Fig. 1a. The output from NEMO
463 corresponding to the same months and same equivalent year (for the second cycle of CORE forcing) in the simulation was
464 selected for both "Closed" (prescribed freshwater flux) and "Open" (FRIS, LCIS and RIS) cavity runs. A comparison
465 between the CTD data and NEMO can be seen in Figs. 6a to 6f for January 1980 and Fig. 6g to 6l for February to March
466 1995. In terms of surface waters, NEMO does not capture the fine scale horizontal variability and overestimates the
467 subsurface salinity. For both observational years, evidence of warm, fresh, MCDW intrusions can be seen in the middle of
468 the CTD sections (Central Trough; Figs. 6a and 6g). While the model struggles to capture the coherence of this sub-surface
469 temperature maximum, the counterclockwise circulation cell set up on the central continental shelf in the open cavity
470 simulation does aid the advection of MCDW towards the ice shelf, thereby producing a slightly better representation of this
471 warm intrusion in Figs. 6c and 6i. The presence of cold ISW in Filchner Trough is clearer in the 1995 CTD data than in 1980
472 where the sampling frequency was sparser and this region not well covered. The 2018 Polarstern sampling of the Jason
473 Trough was the highest resolution yet and while we cannot directly compare with the simulation output as the CORE forcing
474 ends in 2009, the presence of a tongue of ISW focused on the western bank of Filchner Trough is evident in Fig. 3 of Janout
475 et al. (2021) and so should be kept in mind for comparison. Opening the FRIS cavity overall improves the thermohaline
476 properties at the ice shelf front, most notably by spreading out the pool of HSSW from the Ronne Depression (e.g. Fig. 6k)
477 across the continental shelf (e.g. Fig. 6l) and by facilitating the production and thus outflow of ISW within Filchner Trough
478 (Figs. 6c and 6i).
479
480 The CTD sections used for comparison along the front of RIS were obtained through the World Ocean Circulation
481 Experiment Database (Boyer et al., 2018) and correspond to cruises undertaken on board the RVIB Nathaniel B. Palmer in
482 2000 (cruise id: US010404; Smethie and Jacobs, 2005) and in 2007 (cruise id: US034357). Data was extracted from the
483 eORCA1 simulation corresponding to the dates of these cruises and the approximate ship track across the ice shelf front
484 (magenta dotted line in Fig. 1b). Similar to the Weddell Sea, the model tends to overestimate the subsurface temperature and
485 salinity (Figs. 7b, 7e, 7h and 7k), suggestive of biases in the representation of coastal processes, including vertical mixing.
486 This effect is somewhat reduced by allowing for circulation under RIS, especially by decreasing subsurface salinities
487 (Figures 7f and 7l). At depth, NEMO captures the east-west distribution of haline properties such as the HSSW pool located
488 within Joides Basin, albeit with somewhat amplified salinities. In terms of temperature, the model has a clear bias to the east,
489 especially in the closed cavity run, where CDW is detected at the ice shelf front. Both the temperature and salinity biases are
490 reduced in the open cavity run (e.g. Figs. 7c and 7f). In particular, the significant reduction in the extent and magnitude of
491 the sub-surface warm water intrusions brings the model more in-line with observations.
492
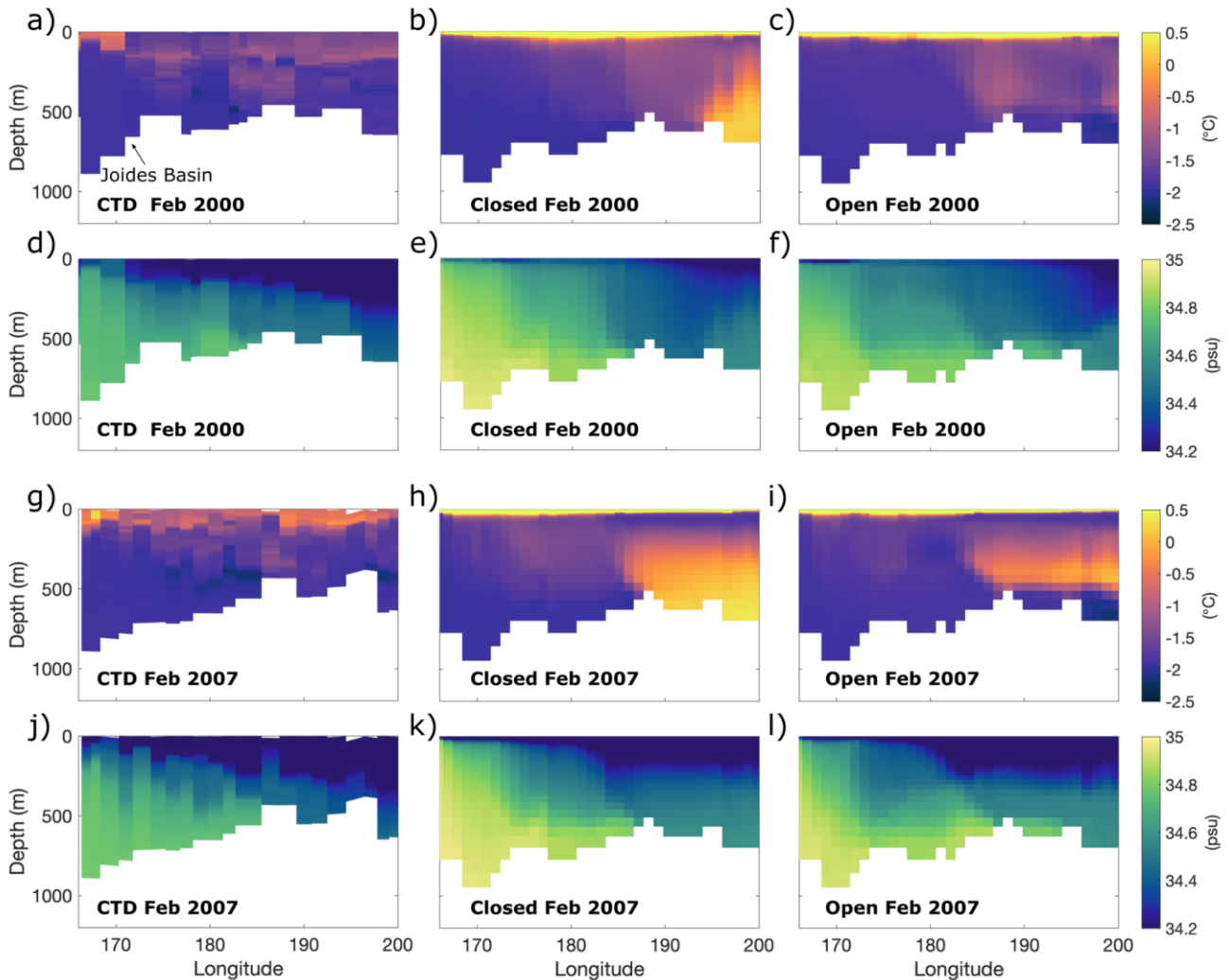
493
494
Figure 7: Same as Fig. 7 but for Ross Ice Shelf front for CTD sections performed in 2000 (Smethie and Jacobs, 2005) and
2007 (Boyer et al., 2018).

497

A recurring theme throughout the results presented here is that the model is overall too salty, driven by what appears to be an
over-production of HSSW in the Ronne Depression and Joides Basin. One driver for this could be the overestimated polynya
activity which forms the totality of parent waters of AABW in the absence of ice shelves in eORCA1. This can be seen in
Fig. 8 where the mean winter (July-August-September) mixed layer depths (MLD) in the reference run for the years 1971-
2009 are compared to the climatology from Sallee et al. (2021) for the same time period and using the same criteria for
calculation (Fig. 8a and 8b; MLD defined as the depth at which density exceeds the 10 m density by 0.03 kg m^{-3}). The model
greatly overestimates winter MLDs in the Weddell Sea, both on the continental shelf adjacent to FRIS, where the depth of
the base of the mixed layer aligns with bathymetric features indicating deep convection right to the ocean floor, and offshore
of the continental slope where a large region of MLD greater than 1000m is present (Fig. 8c). This level of open ocean deep

507 convection has in reality only once been observed, during the 1974-1976 Weddell Polynya event near Maud Rise (3º E, 66º
508 S), indicating a gross overestimation of winter MLDs in the model (Heuze et al., 2021; Killworth et al., 1983). Ross Sea
509 MLDs (Fig. 8d) compare better with observations, but show values indicating a full water-column-depth convection in Terra
510 Nova Bay which is not reported in Sallee at al. (2021). Curiously, NEMO actually under-estimates winter mixed layers in the
511 eastern portion of the Ross continental shelf showing mean MLDs of under 100m where the observational climatology
512 indicates values of around 400m (Fig. 8d compared to Fig. 8b). This too-strong stratification could be one of the factors
513 facilitating the intrusion of CDW to the ice shelf front seen in Figs. 7b and 7h.
514
515 The authors note that the biased MLDs could be one of a number of factors contributing to the overly saline conditions;
516 wrong sea-ice parameters and biases in the atmospheric forcing could also play an important (and related) role. High sea ice
517 production is seen on the southwest continental shelves of the Weddell and Ross Seas in Supplementary Figs. S2a and S2b.
518 Opening the cavities slightly reduces the magnitude of ice production in the Ronne Depression (Fig. S2c) and at the location
519 of the Terra Nova Bay Polynya (Fig. S2d) and increases the production of ice further east. There is no overall change in the
520 principal location of polynya activity and the slight west/east decrease/increase in sea ice is presumed to have a negligible
521 effect on the total amount of HSSW generated. As such, the reduction of the highly saline HSSW signature seen in Figs. 2g
522 and 3g when cavities are opened is likely due to a conversion to ISW (and not from a decrease in HSSW production itself).
523 Please see the Supplementary Information Sect. 3 for an evaluation of simulated polynyas near the studied ice shelves and a
524 diagnosis of the effect of opening the cavities on ice production.
525
526 Once a model is able to explicitly form the parent waters of AABW in the right locations on the continental shelf (and export
527 this dense water), it will become necessary for modelers to tone-down open ocean deep convection as this workaround will
528 be longer relied upon to form the totality of AABW. Here we explore the impact that opening the cavities has on MLD to
529 diagnose the extent of vertical convection in the model. Some reduction in MLD is seen on the continental shelf and slope in
530 the Filchner (Fig. 8e) and Challenger Troughs (Fig. 8f) due to the increase in stratification as a result of the greater bottom
531 densities associated with outflowing ISW (Fig. S4a and S4c). The presence of ISW appears to promote slightly increased ice
532 production in these areas, as discussed earlier. In this case, it is therefore the ocean properties that drive sea ice and the brine
533 rejection associated with elevated ice production is found to have a minor effect on water properties. Within the region of
534 exaggerated MLDs off the Weddell continental slope, the MLDs deepen in the "Open" cavity experiment (positive
535 anomalies Figs. 8e). We hypothesise that this deepening is associated with an overall cooling of the subsurface layers due to
536 a horizontal mixing of ISW, unimpeded by a relatively weak and diffuse Antarctic Slope Current (discussed in the following
537 section). Overall, in wintertime, mixed layers are on average 19 m deeper over the whole Weddell Sea region in the "Open"
538 cavity experiment compared to the reference "Closed" simulation. This reinforcement of the high MLD bias highlights the
539 need for work to be done on reducing wintertime deep convection, together with better representing dense water overflows.
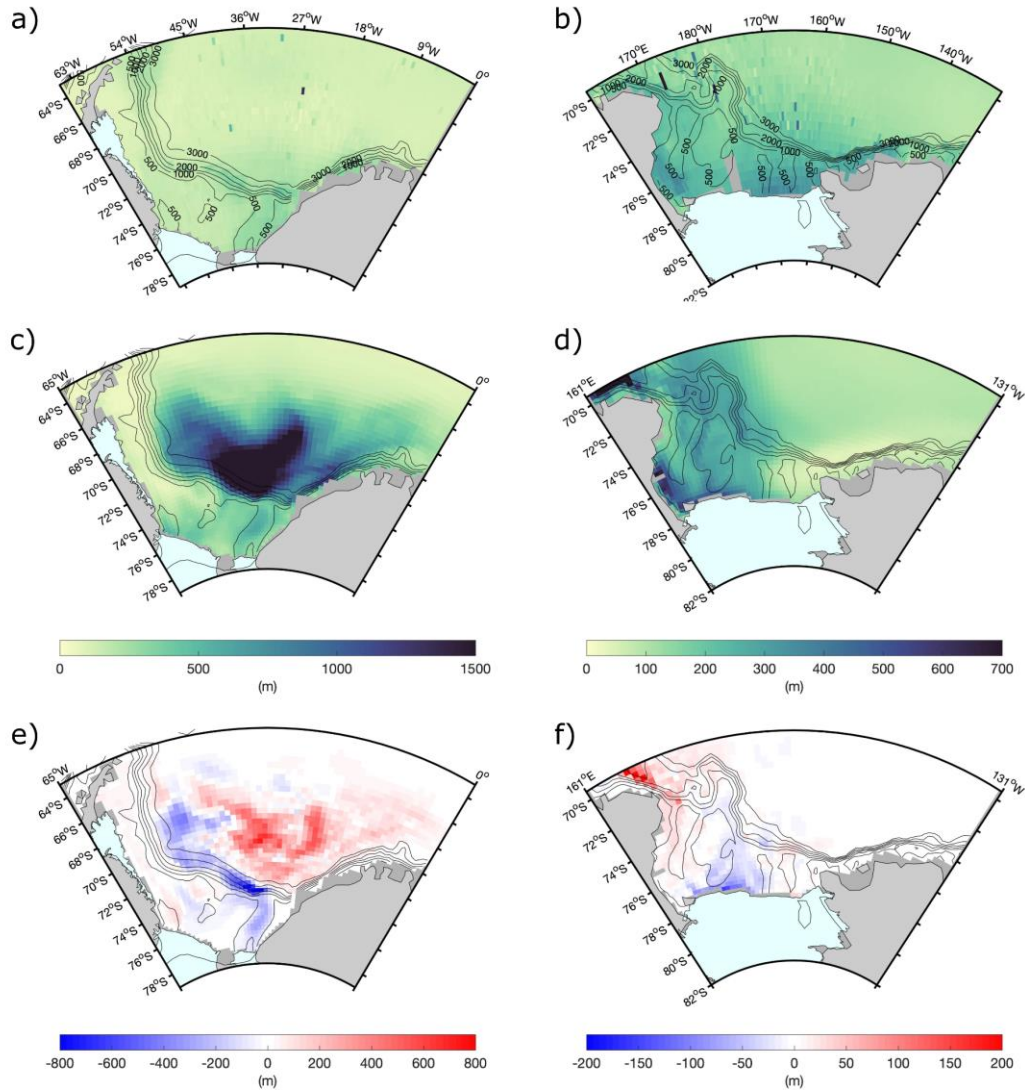
Figure 8: Winter mixed layer depths (MLD) from observational atlas of Sallee et al. (2021) shown in (a) and (b) for the Weddell and Ross Sea respectively, are compared with the winter mean from NEMO v4.2 eORCA1 forced model reference configuration equivalent years 1971-2009 in (c) and (d). The differences in MLDs between the "Open" cavity run and reference "Closed" run are shown in subplots (e) and (f).

4.5 Offshore export of continental shelf properties

We have seen how opening the large, cold, ice shelf cavities in eORCA1 leads to a better representation of continental shelf circulation and thermohaline property distributions. But the question remains regarding the transfer of these now more realistic dense shelf waters downslope and offshore, to feed the globally important AABW. While the simulation period of

552   124 years (two CORE forcing cycles) is too short to explore the impact of these changes far afield, it is sufficient to
553   investigate the changes on the continental shelf and slope adjacent to the large ice shelves. To do this, we use PAGO
554   (Deshayes et al., 2014) to select a cross section of data following the bathymetric troughs of the Weddell and Ross Seas
555   which are thought to be important for dense water export (Foldvok et al., 1985; Jacobs, 1991), namely the Filchner and
556   Challenger Troughs (sections shown in green in Fig. 1).
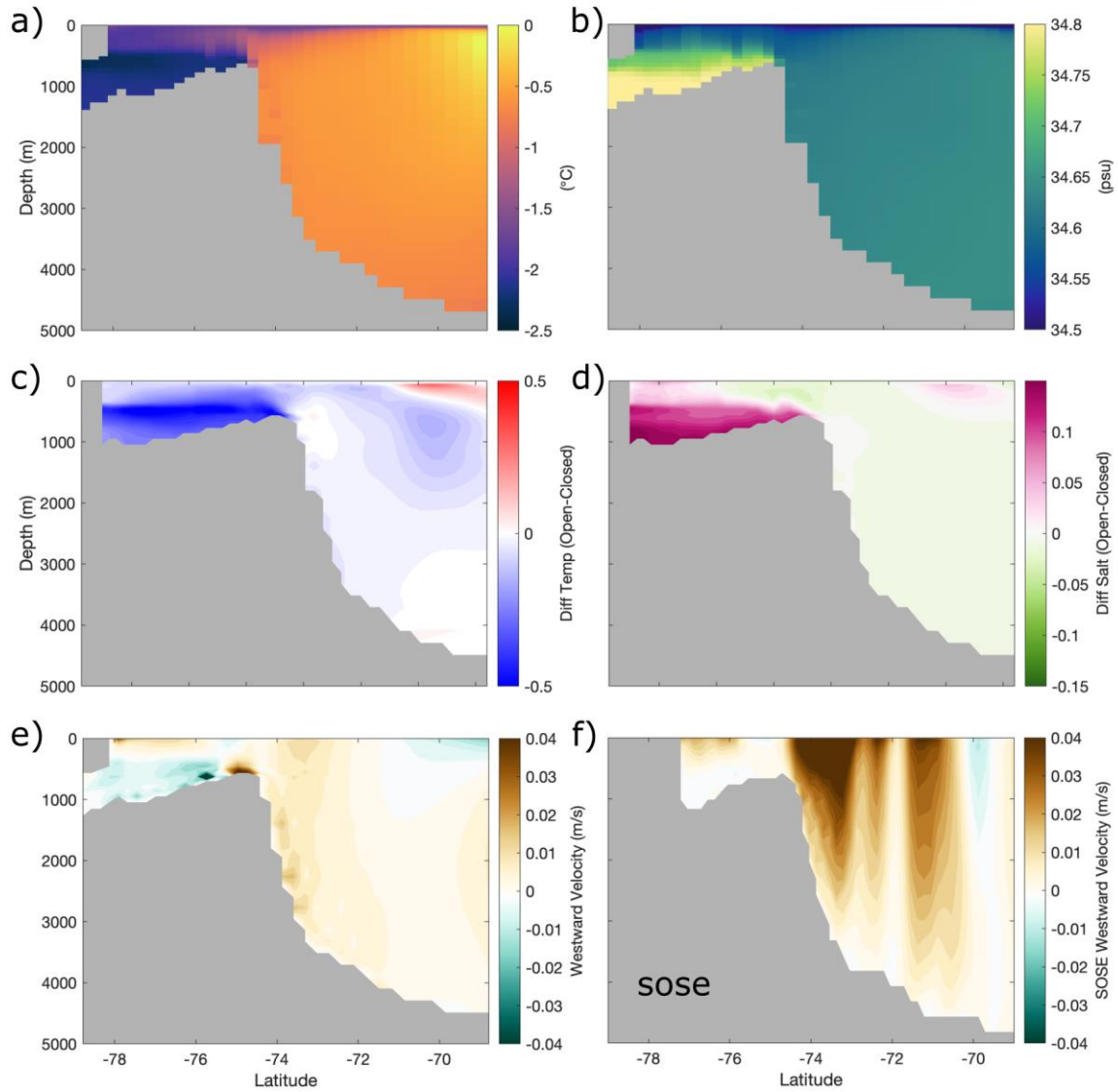
557
558 Figure 9: Cross section of properties along the Filchner Trough and down the adjacent continental slope of the Weddell Sea
559 for (a)-(e) NEMO and (f) SOSE. Subplots (a) and (b) show temperature and salinity for the open cavity configuration, to be
560 compared to (c) and (d) which show the differences (Open - Closed) with the reference configuration. Subplot (e) shows
561 cross sectional velocities with westward as positive for the open cavity run, to be compared with SOSE values shown in
562 subplot (f).
563

564   The thermohaline cross sections of Filchner Trough and a continuation down the continental slope can be seen in Figs. 9a
565   and 9b for the open cavity run and the difference between these values and the reference run (Open-Closed) are shown in
566   Figs. 9c and 9d. By opening the sub-ice shelf cavity, the properties within Filchner Trough have decreased in temperature
567   and increased in salinity as the candidate parent waters of AABW build up on the continental shelf. This results in a net
568   increase in density at the bottom of the trough (Fig. S4b), but there is very little indication of a coherent cascading of this
569   water down the continental slope.
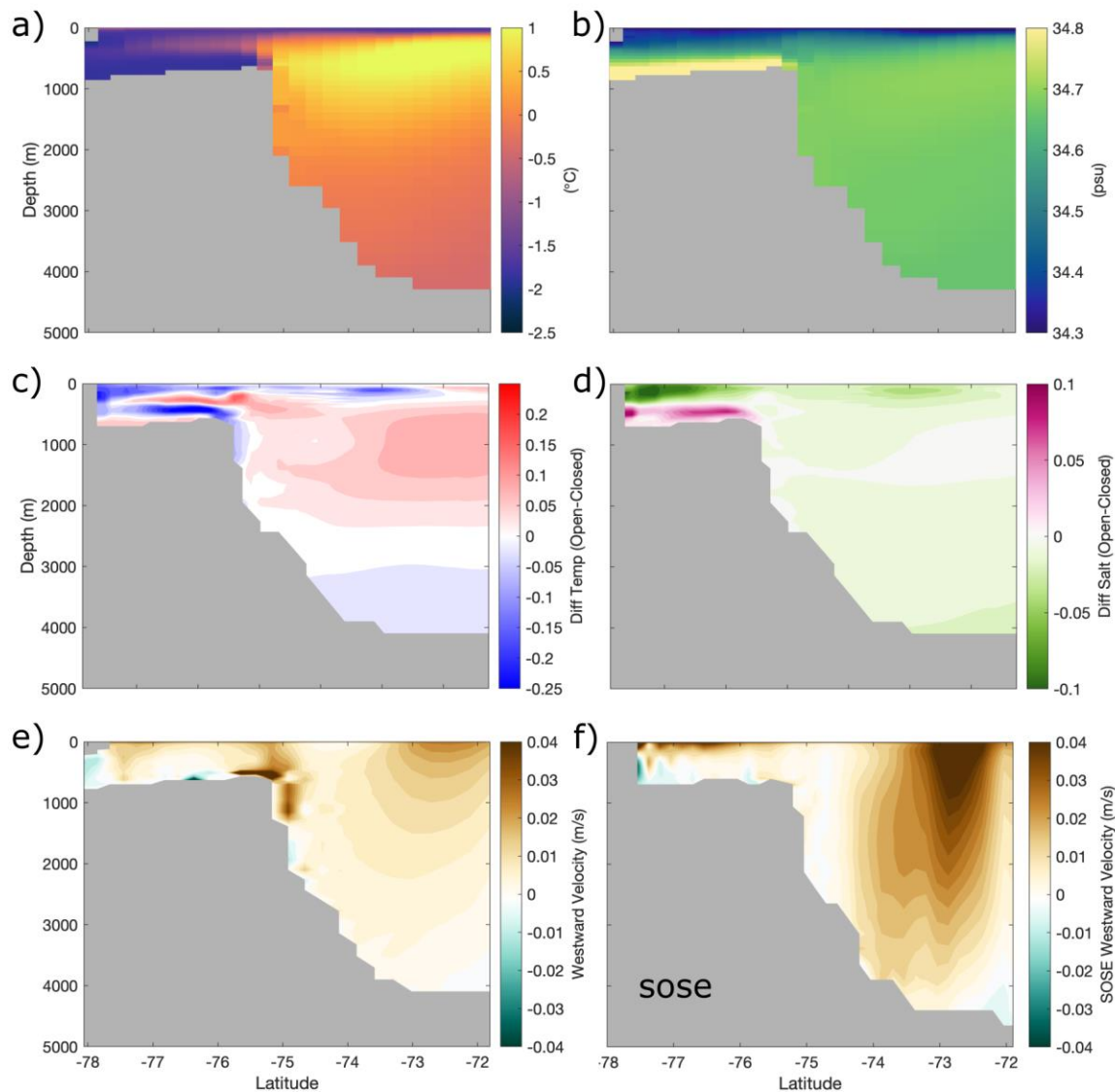
570
571
572   Figure 10: Same as Fig. 9 but for the Challenger Trough and the Ross Sea continental slope.

573
574   A cross section of the Challenger Trough (Fig. 10) reveals depth-varying thermohaline changes. Opening the sub-ice shelf
575   cavity has allowed for the water adjacent to the ice shelf to advect into the cavity leaving the bottom properties here slightly

warmer. The layer immediately above conversely experiences cooling and salinification due to the outflow of ISW driven by the 'ice pump' (Fig. 10c). Here we see some evidence indicating the translation of this dense cold water tongue over the continental shelf break and downslope (Figs. 10c and S4d). The overflow of this water results in the pulling in of warmer offshore water at intermediate depth (Fig. 10c). A horizontal redistribution of surface waters simultaneously takes place due to the anti-clockwise circulation pattern (Fig. 5e) which in turn produces a cooling and freshening in the surface layer (Figs. 10c and 10d).

For both the Filchner and Challenger Troughs, the downslope export of the ISW tongue is limited due to the commonly-known and acknowledged problem of correctly capturing this overflow in a coarse z-coordinate model (Heuze et al., 2021). The aptitude of representing dense water overflows is thought to increase with models of higher resolution, but this is difficult to achieve in a global model for climate coupling purposes without a nested zoom (Storkey et al., 2018; Colombo et al., 2020; Solodoch et al., 2022).

Another important dynamic for Antarctic shelf water realism is the ASC (red arrows in Fig. 1) and related Antarctic Slope Front, which together restrict the lateral mixing of offshore and shelf water masses, acting as an effective barrier protecting the large cold ice shelves from warm water masses of circumpolar origin (Thompson et al., 2018). Some CDW, or a modified version thereof, is carried within the ASC and occasionally fluxes onshore to mix with dense shelf waters (Beadling et al., 2020; Bull et al., 2021). This interaction between dense shelf water and CDW is important for the formation of AABW, as the onshore flux of water replaces the dense water transported offshore and thus sustains formation of shelf water (Thompson et al., 2018). Figure 9e shows a velocity cross section for the Weddell Sea shelf and slope where westward velocities are positive so as to correspond with the direction of the ASC and the net westward transport across the section is 9.8 Sv (1 Sv is 10^6 m^3 s^{-1}). This can be compared to Fig. 9f which is a cross section from SOSE output (same time periods used) where the net transport is three times higher at 32.8 Sv. Similarly for the Ross Sea, Fig. 10e shows a cross section of westward velocities in eORCA1 where the volume transport is 13.3 Sv which is less than half of that estimated from SOSE in Fig. 10f of 20.9 Sv. As can be seen from both SOSE cross sections, the ASC flows eastward as a narrow jet, closely following the shelf break in the Weddell Sea and slightly further offshore in the Ross Sea. It is well known that coarse resolution models are unable to correctly represent the ASC as a resolution of at least 0.5° is needed to capture the dynamics and net transport (Mathiot et al., 2011). The absence of realistic ASC in NEMO eORCA1 (Figs. 9e and 10e) has important consequences, as a weaker and more diffuse ASC allows for a greater level of onshore-offshore exchange of water masses. This is one important restriction that needs to be kept in mind when using this coarse resolution configuration for process studies in the area.

5 Summary and Discussion

Explicitly representing ocean-ice shelf interactions is of great interest to modelers as these processes play an important role in global ocean dynamics, climate and future sea level rise. The formation of dense shelf waters (HSSW and ISW) along the Antarctic coastline provides the principal source for AABW, which in turn facilitates the ventilation of the deep ocean and constitutes the lower limb of the global overturning circulation (Killworth, 1983; Johnson, 2008; Orsi, 2010).

Our results focus on the Weddell and Ross seas as they are respectively the main ventilation source of the abyssal Atlantic and Indian basins, and the abyssal Pacific basin (Solodoch et al., 2022). Explicitly simulating the sub-ice shelf cavities of FRIS and LCIS in the Weddell Sea leads to a re-organisation of continental shelf circulation with thermohaline patterns in agreement with those reported by other NEMO model studies (Mathiot et al., 2017; Storkey et al., 2018 and Bull et al., 2021), namely warming and freshening in the west and cooling and salinification in the east. Notably, opening a pathway for

620 HSSW under FRIS allows for an anticlockwise circulation of water under the ice shelf, triggering basal melt and re-freezing,
621 and producing the super-cold ISW.

623 By comparing model output with two CTD sections performed across the front of FRIS in 1980 and 1995 (Rohardt et al.,
624 2016; Janout et al., 2021), we see clear evidence of an improvement in the realism of water properties with the opening of
625 the sub-ice shelf cavity. Similarly in the Ross Sea, an anticlockwise sub-ice shelf cavity circulation cell facilitates the spread
626 of HSSW across the continental shelf and ocean-ice shelf interactions create a cold ISW plume to the east of Roosevelt
627 Island. By evaluating the model output against CTD sections performed in 2000 and 2007 (Smethie and Jacobs, 2005; Boyer
628 et al., 2018), we see that opening the cavity significantly ameliorates the sub-surface warm water bias otherwise seen to the
629 east of RIS in the reference configuration, and brings a significant improvement in the horizontal thermohaline distributions.

631 The mean total melt fluxes of FRIS, LCIS and RIS are found to be within the uncertainty range of observational estimates
632 and other model studies. Notably, the melt rate pattern of FRIS agrees surprisingly well with the high resolution regional
633 model of Haussmann et al. (2020) and the satellite observations of Rignot et al. (2013), showing details of melt and
634 refreezing that were not expected at a 1° resolution, although the meanders of the grounding line are not well represented at
635 1°. For RIS, the net melt is higher than all observed estimates but lower than that predicted by other model studies. RIS melt
636 rates are strongly related to the supply of warm water to the ice shelf base (Arzeno et al., 2014), and correctly representing
637 this in models presents a challenge due to the close proximity of CDW to the ice shelf front in this area.

639 Meltwater and modified HSSW mix on the continental shelves of the Weddell and Ross Sea and in reality cascade down the
640 continental slope, mixing with ambient water masses during the descent, to eventually feed AABW. This process is poorly
641 represented in NEMO eORCA1, a common problem with coarse z-coordinate models, as exaggerated vertical and horizontal
642 mixing erodes the signatures of the dense overflow tongue. As mentioned by Storkey et al. (2018), the use of a terrain
643 following coordinate system (known as sigma coordinate) can greatly improve the representation of these density currents,
644 and so is something worth exploring in the future. Improvement in the representation of the overflows along with a reduction
645 of open-ocean deep convection should together allow for a coherent communication of the now more realistic properties of
646 dense water on the continental shelf offshore to AABW.

648 **6 Conclusion**

650 In this paper the authors focus on improving the properties of AABW parent waters in a global NEMO configuration. We
651 compare the model simulations with in situ observations, in addition to gridded climatologies, so as to deepen understanding
652 and expertise regarding the impact of opening sub-ice shelf cavities on ocean dynamics. As ocean models used for climate
653 simulations with multiple scenarios (such as CMIP) need to be at a coarse resolution to permit long integrations, we use the
654 NEMO global ocean 1° configuration, eORCA1, here. The results presented are for CORE inter-annual forcing, with a fixed
655 cavity geometry, as this allows us to clearly identify the impact of ocean-ice shelf interactions at a few critical locations
656 without the obscuring effect of coupling feedbacks. We present here a validated configuration of NEMO 4.2 eORCA1 with
657 explicit ocean-ice shelf interactions only within the largest 3 cold cavities: FRIS, LCIS and RIS. Limitations of this choice
658 are that together FRIS, LCIS and RIS only represent 63 % of the total area of Antarctic ice shelves and, while they are
659 responsible for the formation of the majority of the parent waters of AABW, interactions with remote unresolved ice shelves
660 are missing (Nakayama et al., 2020). The next steps in terms of increasing complexity in NEMO eORCA1 are to open other
661 intermediate size cavities, such as Amery, Riiser-Larsen and Fimbul, in a fixed geometry configuration, and leave smaller
662 cavities parameterized due to resolution constraints. As the residence time needed to flush these intermediate cavities is
663 shorter than for FRIS and RIS, we suggest that the complex initialization methods presented here are not needed. This work

is aimed at building understanding so as to eventually move to coupling with an ice sheet model thereby allowing for fully evolving cavity geometry and iceberg calving from the ice shelf front.

Given the critical role that the Southern Ocean plays in regulating global climate, it is paramount that ocean models work towards improving the representation of key processes in order to provide state-of-the-art simulations of the ocean in a changing climate (Beadling et al., 2020). The global configuration of NEMO presented here, has been proven to improve the realism of water masses in the Weddell and Ross Seas. We advocate for climate modelers to use it, as it enables a more accurate representation of the formation of the parent waters of AABW, and a first step in the perspective of representing ocean-ice shelf interactions in climate applications.

7 Author contribution

KH, JD and PM together contributed to the conceptualization of the research outlined in this manuscript. KH led the formal analysis and investigation with the assistance of JD, CR, CL, NJ and PM. MV led the sea ice research component with assistance from CR and CL. Validation of the model was undertaken by KH with PM. CE led the programming, code management and supervised all the model runs undertaken by KH. The project was supervised by JD and NJ, providing guidance and critical feedback. The whole group contributed to the writing and review of the submitted manuscript.

8 Competing interests

The authors declare that they have no conflict of interest.

9 Acknowledgements of financial support

Katherine Hutchinson received financial support of the European Union's Horizon 2020 research and innovation programme Marie Skłodowska-Curie grant agreement No 898058 (Project OPEN). Nicolas Jourdain received support from the European Union's Horizon 2020 research and innovation programme under grant agreement no. 101003536 (ESM2025). Pierre Mathiot acknowledges support from the European Union's Horizon 2020 research and innovation programme under grant agreement no. 820575 (TiPACCs). This work was performed using HPC resources from GENCI–IDRIS (Grant 2021-A0100107451) and from the IPSL Mesocentre ESPRI.

10 Code and data availability

The NEMO ocean model code is available via open software license from the NEMO website (https://www.nemo-ocean.eu). The NEMO output for the Weddell and Ross Seas (focus of this study), plus the namelists used, bathymetry, ice shelf draft, freshwater input and initial condition files are available via the data repository stored here: https://doi.org/10.5281/zenodo.7561767. Some example scripts for data extraction, calculations and plotting can also be found in this repository. The World Ocean Atlas hydrographic data of Locarnini et al. (2019) and Zweng et al. (2019) can be found here: https://www.nodc.noaa.gov/OC5/woa18/woa18data.html and Southern Ocean State Estimate data of Mazloff et al. (2010) can be accessed here: http://sose.ucsd.edu/sose_stateestimation_data_05to10.html. The mixed layer depth data from Sallee et al. (2021) can be accessed here: https://doi.org/10.5281/zenodo.5776180. The CTD transects used for comparisons across the ice shelf front for FRIS 1980 and 1995 can be respectively found here: https://doi.org/10.1594/PANGAEA.860066 and here https://folk.uib.no/ngfso/Data/CTD/. The RIS CTD data from the 2000

708   (US010402) and 2007 (US034357) RVIB Nathaniel B. Palmer cruises are available from the World Ocean Data Base at

709   https://www.nodc.noaa.gov/OC5/WOD/pr_wod.html. The PAGO toolbox used to extract model output along a line in front

710   of the ice shelf from Deshayes et al. (2014) can be accessed here: https://www.whoi.edu/science/PO/pago/.

711   **References**

712   Arndt, J. E., Schenke, H. W., Jakobsson, M., Nitsche, F. O., Buys, G., Goleby, B., Rebesco, M., Bohoyo, F., Hong, J. and

713   Black, J.: The International Bathymetric Chart of the Southern Ocean (IBCSO) Version 1.0—A new bathymetric

714   compilation covering circum-Antarctic waters, Geophys.Res.Lett. 12, 2013.

715   Asay-Davis, X. S., Cornford, S. L., Durand, G., Galton-Fenzi, B. K., Gladstone, R. M., Gudmundsson, G. H., Hattermann,

716   T., Holland, D. M., Holland, D. and Holland, P. R.: Experimental design for three interrelated marine ice sheet and ocean

717   model intercomparison projects: MISMIP v. 3 (MISMIP), ISOMIP v. 2 (ISOMIP) and MISOMIP v. 1 (MISOMIP1),

718   Geoscientific Model Development 7, 2016.

719   Beadling, R. L. L., Russell, J. L., Stouffer, R., Mazloff, M. R., Talley, L. D., Goodman, P. J., Sallee, J. B., Hewitt, H., Hyder,

720   P. and Pandde, A.: Simulation of Southern Ocean Properties Across Model Generations and Future Changes under

721   Continued 21 st Century Warming in CMIP6. 2020.

722   Bergamasco, A., Defendi, V., Zambianchi, E. and Spezie, G.: Evidence of dense water overflow on the Ross Sea shelf-break,

723   Antarct.Sci. 3, 2002.

724   Bergamasco, A., Defendi, V., Del Negro, P. and Umani, S. F.: Effects of the physical properties of water masses on

725   microbial activity during an Ice Shelf Water overflow in the central Ross Sea, Antarct.Sci. 3, 2003.

726   Bitz, C. M., Holland, M. M., Weaver, A. J. and Eby, M.: Simulating the ice-thickness distribution in a coupled climate

727   model, Journal of Geophysical Research: Oceans C2, 2001.

728   Bowen, M. M., Fernandez, D., Forcen-Vazquez, A., Gordon, A. L., Huber, B., Castagno, P. and Falco, P.: The role of tides

729   in bottom water export from the western Ross Sea, Scientific reports 1, 2021.

730   Boyer, T.P., O.K. Baranova, C. Coleman, H.E. Garcia, A. Grodsky, R.A. Locarnini, A.V. Mishonov, C.R. Paver, J.R.

731   Reagan, D. Seidov, I.V. Smolyar, K. Weathers, M.M. Zweng. : World Ocean Database 2018. A.V. Mishonov, Technical Ed.,

732   NOAA Atlas NESDIS 87, 2018.

733   Budillon, G., Pacciaroni, M., Cozzi, S., Rivaro, P., Catalano, G., Ianni, C. and Cantoni, C.: An optimum multiparameter

734   mixing analysis of the shelf waters in the Ross Sea, Antarct.Sci. 1, 2003.

735   Bull, C. Y., Jenkins, A., Jourdain, N. C., Vaňková, I., Holland, P. R., Mathiot, P., Hausmann, U. and Sallée, J.: Remote

736   Control of Filchner-Ronne Ice Shelf Melt Rates by the Antarctic Slope Current, Journal of Geophysical Research: Oceans 2,

737   2021.

738   Burgard, C., Jourdain, N. C., Reese, R., Jenkins, A. and Mathiot, P.: An assessment of basal melt parameterisations for

739   Antarctic ice shelves, The Cryosphere 12, 2022.

740   Cao, J., Wang, B., Yang, Y., Ma, L., Li, J., Sun, B., Bao, Y., He, J., Zhou, X. and Wu, L.: The NUIST Earth System Model

741   (NESM) version 3: description and preliminary evaluation, Geoscientific Model Development 7, 2018.

742   Colombo, P., Barnier, B., Penduff, T., Chanut, J., Deshayes, J., Molines, J., Le Sommer, J., Verezemskaya, P., Gulev, S. and

743   Treguier, A.: Representation of the Denmark Strait overflow in a z-coordinate eddying configuration of the NEMO (v3. 6)

744   ocean model: resolution and parameter impacts, Geoscientific Model Development 7, 2020.

745 Comeau, D., Asay-Davis, X. S., Begeman, C. B., Hoffman, M. J., Lin, W., Petersen, M. R., Price, S. F., Roberts, A. F., Van
746 Roekel, L. P. and Veneziani, M.: The DOE E3SM v1. 2 Cryosphere Configuration: Description and Simulated Antarctic Ice-
747 Shelf Basal Melting, Journal of Advances in Modeling Earth Systems 2, 2022.

748 de Lavergne, C., Vic, C., Madec, G., Roquet, F., Waterhouse, A. F., Whalen, C. B., Cuypers, Y., Bouruet-Aubertot, P.,
749 Ferron, B. and Hibiya, T.: A parameterization of local and remote tidal mixing, Journal of Advances in Modeling Earth
750 Systems 5, 2020.

751 Depoorter, M. A., Bamber, J. L., Griggs, J. A., Lenaerts, J. T., Ligtenberg, S. R., van den Broeke, M. R. and Moholdt, G.:
752 Calving fluxes and basal melt rates of Antarctic ice shelves, Nature 7469, 2013.

753 Deshayes, J., Curry, R. and Msadek, R.: CMIP5 model intercomparison of freshwater budget and circulation in the North
754 Atlantic, J.Clim. 9, 2014.

755 Dufresne, J., Foujols, M., Denvil, S., Caubel, A., Marti, O., Aumont, O., Balkanski, Y., Bekki, S., Bellenger, H. and
756 Benshila, R.: Climate change projections using the IPSL-CM5 Earth System Model: from CMIP3 to CMIP5, Clim.Dyn. 9,
757 2013.

758 Fahrbach, E., Rohardt, G., Scheele, N., Schröder, M., Strass, V. and Wisotzki, A.: Formation and discharge of deep and
759 bottom water in the northwestern Weddell Sea, J.Mar.Res. 4, 1995.

760 Frölicher, T. L., Sarmiento, J. L., Paynter, D. J., Dunne, J. P., Krasting, J. P. and Winton, M.: Dominance of the Southern
761 Ocean in anthropogenic carbon and heat uptake in CMIP5 models, J.Clim. 2, 2015.

762 Foldvik, A., Gammelsrød, T. and Tørresen, T.: Circulation and water masses on the southern Weddell Sea shelf, Oceanology
763 of the Antarctic continental shelf, 1985.

764 Goosse, H., Dalaiden, Q., Cavitte, M. G. and Zhang, L.: Can we reconstruct the formation of large open-ocean polynyas in
765 the Southern Ocean using ice core records? Climate of the Past 1, 2021.

766 Gordon, A. L. : Interocean exchange of thermocline water, Journal of Geophysical Research: Oceans C4, 1986.

767 Gordon, A. L., Visbeck, M. and Huber, B.: Export of Weddell Sea deep and bottom water, Journal of Geophysical Research:
768 Oceans C5, 2001.

769 Griffies, S. M., Biastoch, A., Böning, C., Bryan, F., Danabasoglu, G., Chassignet, E. P., England, M. H., Gerdes, R., Haak,
770 H. and Hallberg, R. W.: Coordinated ocean-ice reference experiments (COREs), Ocean modelling 1-2, 2009.

771 Harrison, L. C., Holland, P. R., Heywood, K. J., Nicholls, K. W. and Brisbourne, A. M.: Sensitivity of melting, freezing and
772 marine ice beneath Larsen C Ice Shelf to changes in ocean forcing, Geophys.Res.Lett. 4, 2022.

773 Hausmann, U., Sallée, J., Jourdain, N. C., Mathiot, P., Rousset, C., Madec, G., Deshayes, J. and Hattermann, T.: The Role of
774 Tides in Ocean-Ice Shelf Interactions in the Southwestern Weddell Sea, Journal of Geophysical Research: Oceans 6, 2020.

775 Hazeleger, W., Severijns, C., Semmler, T., Ştefănescu, S., Yang, S., Wang, X., Wyser, K., Dutra, E., Baldasano, J. M. and
776 Bintanja, R.: EC-Earth: a seamless earth-system prediction approach in action, Bull.Am.Meteorol.Soc. 10, 2010.

777 Hellmer, H. H. and Olbers, D. J.: A two-dimensional model for the thermohaline circulation under an ice shelf, Antarct.Sci.
778 4, 1989.

779 Hellmer, H. H. : Impact of Antarctic ice shelf basal melting on sea ice and deep ocean properties, Geophys.Res.Lett. 10,
780 2004.

781 Heuzé, C., Heywood, K. J., Stevens, D. P. and Ridley, J. K.: Southern Ocean bottom water characteristics in CMIP5 models,
782 Geophys.Res.Lett. 7, 2013.

783 Heuzé, C. : Antarctic bottom water and North Atlantic deep water in cmip6 models, Ocean Science 1, 2021.

784 Hewitt, H. T., Copsey, D., Culverwell, I. D., Harris, C. M., Hill, R., Keen, A. B., McLaren, A. J. and Hunke, E. C.: Design
785 and implementation of the infrastructure of HadGEM3: The next-generation Met Office climate modelling system,
786 Geoscientific Model Development 2, 2011.

787 Hewitt, H. T., Roberts, M. J., Hyder, P., Graham, T., Rae, J., Belcher, S. E., Bourdallé-Badie, R., Copsey, D., Coward, A.
788 and Guiavarch, C.: The impact of resolving the Rossby radius at mid-latitudes in the ocean: Results from a high-resolution
789 version of the Met Office GC2 coupled model, Geoscientific Model Development 10, 2016.

790 Holland, D. M. and Jenkins, A.: Modeling thermodynamic ice–ocean interactions at the base of an ice shelf,
791 J.Phys.Oceanogr. 8, 1999.

792 Huot, P., Fichefet, T., Jourdain, N. C., Mathiot, P., Rousset, C., Kittel, C. and Fettweis, X.: Influence of ocean tides and ice
793 shelves on ocean–ice interactions and dense shelf water formation in the D'Urville Sea, Antarctica, Ocean Modelling 2021.

794 Hutchinson, K., Deshayes, J., Sallee, J., Dowdeswell, J. A., de Lavergne, C., Ansorge, I., Luyt, H., Henry, T. and Fawcett, S.
795 E.: Water mass characteristics and distribution adjacent to Larsen C Ice Shelf, Antarctica, Journal of Geophysical Research:
796 Oceans 4, 2020.

797 Huthnance, J. M. : Circulation, exchange and water masses at the ocean margin: the role of physical processes at the shelf
798 edge, Prog.Oceanogr. 4, 1995.

799 Jacobs, S. S., Gordon, A. L. and Ardai, J. L.,Jr: Circulation and melting beneath the ross ice shelf, Science, 1979.

800 Jacobs, S. S.: On the nature and significance of the Antarctic Slope Front, Mar.Chem. 1-4, 1991..

801 Janout, M. A., Hellmer, H. H., Hattermann, T., Huhn, O., Sültenfuss, J., Østerhus, S., Stulic, L., Ryan, S., Schröder, M. and
802 Kanzow, T.: FRIS revisited in 2018: On the circulation and water masses at the Filchner and Ronne ice shelves in the
803 southern Weddell Sea, Journal of Geophysical Research: Oceans 6, 2021.

804 Jenkins, A.: A one-dimensional model of ice shelf-ocean interaction, Journal of Geophysical Research: Oceans C11, 1991.

805 Jeong, H., Asay-Davis, X. S., Turner, A. K., Comeau, D. S., Price, S. F., Abernathey, R. P., Veneziani, M., Petersen, M. R.,
806 Hoffman, M. J. and Mazloff, M. R.: Impacts of ice-shelf melting on water-mass transformation in the Southern Ocean from
807 E3SM simulations, J.Clim. 13, 2020.

808 Johnson, G. C. : Quantifying Antarctic bottom water and North Atlantic deep water volumes, Journal of Geophysical
809 Research: Oceans C5, 2008.

810 Jourdain, N. C., Mathiot, P., Merino, N., Durand, G., Le Sommer, J., Spence, P., Dutrieux, P. and Madec, G.: Ocean
811 circulation and sea-ice thinning induced by melting ice shelves in the Amundsen Sea, Journal of Geophysical Research:
812 Oceans 3, 2017.

813 Jourdain, N. C., Molines, J., Le Sommer, J., Mathiot, P., Chanut, J., de Lavergne, C. and Madec, G.: Simulating or
814 prescribing the influence of tides on the Amundsen Sea ice shelves, Ocean Modelling 2019.

815 Kerr, R., Dotto, T. S., Mata, M. M. and Hellmer, H. H.: Three decades of deep water mass investigation in the Weddell Sea
816 (1984–2014): temporal variability and changes, Deep Sea Research Part II: Topical Studies in Oceanography 2018.

817 Killworth, P. D. : Deep convection in the world ocean, Rev.Geophys. 1, 1983.

Kimmritz, M., Danilov, S. and Losch, M.: The adaptive EVP method for solving the sea ice momentum equation, Ocean Modelling 2016.

Large, W. G. and Yeager, S. G.: Diurnal to decadal global forcing for ocean and sea-ice models: the data sets and flux climatologies. CGD Division of the National Center for Atmospheric Research, NCAR Technical Note: NCAR/TN-460+STR. 2004.

Lipscomb, W. H. : Remapping the thickness distribution in sea ice models, Journal of Geophysical Research: Oceans C7, 2001.

Locarnini, M. M., Mishonov, A. V., Baranova, O. K., Boyer, T. P., Zweng, M. M., Garcia, H. E., Seidov, D., Weathers, K., Paver, C. and Smolyar, I.: World Ocean Atlas 2018, volume 1: Temperature, 2018.

Locarnini, R. A., A. V. Mishonov, J. I. Antonov, T. P. Boyer, H. E. Garcia, O. K. Baranova, M. M. Zweng, C. R. Paver, J. R. Reagan, D. R. Johnson, M. Hamilton, and D. Seidov. : World Ocean Atlas 2013, 2013.

Losch, M. : Modeling ice shelf cavities in a z coordinate ocean general circulation model, Journal of Geophysical Research: Oceans C8, 2008.

Madec, G. and NEMO System Team: Nemo ocean engine, Scientific Notes of Climate Modelling Center (27) – ISSN 1288-1619, Institut Pierre-Simon Laplace (IPSL) 10.5281/zenodo.3878122, 2019.

Marshall, J. and Speer, K.: Closure of the meridional overturning circulation through Southern Ocean upwelling, Nature Geoscience 3, 2012.

Mathiot, P., Goosse, H., Fichefet, T., Barnier, B. and Gallée, H.: Modelling the seasonal variability of the Antarctic Slope Current, Ocean Science 4, 2011.

Mathiot, P., Jenkins, A., Harris, C. and Madec, G.: Explicit representation and parametrised impacts of under ice shelf seas in the z* coordinate ocean model NEMO 3.6, Geoscientific Model Development 7, 2017.

Mazloff, M. R., Heimbach, P. and Wunsch, C.: An eddy-permitting Southern Ocean state estimate, J.Phys.Oceanogr. 5, 2010.

Menviel, L., Timmermann, A., Timm, O. E. and Mouchet, A.: Climate and biogeochemical response to a rapid melting of the West Antarctic Ice Sheet during interglacials and implications for future climate, Paleoceanography 4, 2010.

Meredith, M., Sommerkorn, M., Cassotta, S., Derksen, C., Ekaykin, A., Hollowed, A., Kofinas, G., Mackintosh, A., Melbourne-Thomas, J., Muelbert, M.M.C. and Ottersen, G. : Polar regions. IPCC Special Report on the Ocean and Cryosphere in a Changing Climate, IPCC https://www.ipcc.ch/srocc/chapter, p.2., 2019.

Merino, N., Le Sommer, J., Durand, G., Jourdain, N. C., Madec, G., Mathiot, P. and Tournadre, J.: Antarctic icebergs melt over the Southern Ocean: Climatology and impact on sea ice, Ocean Modelling, 2016.

Moholdt, G., Padman, L. and Fricker, H. A.: Basal mass budget of Ross and Filchner-Ronne ice shelves, Antarctica, derived from Lagrangian analysis of ICESat altimetry, Journal of Geophysical Research: Earth Surface 11, 2014.

Mohrmann, M., Heuzé, C. and Swart, S.: Southern Ocean polynyas in CMIP6 models, The Cryosphere 9, 2021.

Nakayama, Y., Timmermann, R. and H Hellmer, H.: Impact of West Antarctic ice shelf melting on Southern Ocean hydrography, The Cryosphere 7, 2020.

854   Naughten, K. A., Meissner, K. J., Galton-Fenzi, B. K., England, M. H., Timmermann, R., Hellmer, H. H., Hattermann, T.
855   and Debernard, J. B.: Intercomparison of Antarctic ice-shelf, ocean, and sea-ice interactions simulated by MetROMS-
856   iceshelf and FESOM 1.4, Geoscientific Model Development 4, 2018.

857   Naughten, K. A., De Rydt, J., Rosier, S. H., Jenkins, A., Holland, P. R. and Ridley, J. K.: Two-timescale response of a large
858   Antarctic ice shelf to climate change, Nature communications 1, 2021.

859   Naveira Garabato, A. C., McDonagh, E. L., Stevens, D. P., Heywood, K. J. and Sanders, R. J.: On the export of Antarctic
860   bottom water from the Weddell Sea, Deep Sea Research Part II: Topical Studies in Oceanography 21, 2002.

861   NEMO System Team: NEMO ocean engine, scientific notes of climate modelling center, 27, ISSN 1288-1619 Institut
862   Pierre-Simon Laplace (IPSL), 10.5281/zenodo.6334656, 2022.

863   Nicholls, K. W., Østerhus, S., Makinson, K. and Johnson, M. R.: Oceanographic conditions south of Berkner Island, beneath
864   Filchner-Ronne Ice Shelf, Antarctica, Journal of Geophysical Research: Oceans C6, 2001.

865   Nicholls, K. W., Pudsey, C. J. and Morris, P.: Summertime water masses off the northern Larsen C Ice Shelf, Antarctica,
866   Geophys.Res.Lett. 9, 2004.

867   Nicholls, K. W., Østerhus, S., Makinson, K., Gammelsrød, T. and Fahrbach, E.: Ice-ocean processes over the continental
868   shelf of the southern Weddell Sea, Antarctica: A review, Rev.Geophys. 3, 2009.

869   NOAA: National Geophysical Data Center 2-minute gridded global relief data (ETOPO2) v2, National Geophysical Data
870   Center NOAA, 2006.

871   Orsi, A. H., Johnson, G. C. and Bullister, J. L.: Circulation, mixing, and production of Antarctic Bottom Water,
872   Prog.Oceanogr. 1, 1999.

873   Orsi, A. H. : Recycling bottom waters, Nature Geoscience 5, 2010.

874   Phipps, S. J., Fogwill, C. J. and Turney, C. S.: Impacts of marine instability across the East Antarctic Ice Sheet on Southern
875   Ocean dynamics, The Cryosphere 5, 2016.

876   Prather, M. J. : Numerical advection by conservation of second-order moments, Journal of Geophysical Research:
877   Atmospheres D6, 1986.

878   Rignot, E., Jacobs, S., Mouginot, J. and Scheuchl, B.: Ice-shelf melting around Antarctica, Science 6143, 2013.

879   Rintoul, S. R.: The global influence of localized dynamics in the Southern Ocean, Nature 7709, 2018.

880   Robertson, R., Visbeck, M., Gordon, A. L. and Fahrbach, E.: Long-term temperature trends in the deep waters of the
881   Weddell Sea, Deep Sea Research Part II: Topical Studies in Oceanography 21, 2002.

882   Rohardt, G., Fahrbach, E., Beszczynska-Möller, A., Boetius, A., Brunßen, J., Budéus, G., Cisewski, B., Engbrodt, R.,
883   Gauger, S., Geibert, W., Geprägs, P., Gerdes, D., Gersonde, R., Gordon, A. L., Hellmer, H. H., Isla, E., Jacobs, S. S., Janout,
884   M. A., Jokat, W., Klages, M., Kuhn, G., Meincke, J., Ober, S., Østerhus, S., Peterson, R. G., Rabe, B., Rudels, B., Schauer,
885   U., Schröder, M., Sildam, J., Soltwedel, T., Stangeew, E., Stein, M., Strass, V. H., Thiede, J., Tippenhauer, S., Veth, C., von
886   Appen, W., Weirig, M., Wisotzki, A., Wolf-Gladrow, D. A. and Kanzow, T.: Physical oceanography on board of
887   POLARSTERN (1983-11-22 to 2016-02-14). Alfred Wegener Institute, Helmholtz Centre for Polar and Marine Research,
888   Bremerhaven, 10.1594/PANGAEA.860066, 2016.

889   Sallée, J., Pellichero, V., Akhoudas, C., Pauthenet, E., Vignes, L., Schmidtko, S., Garabato, A. N., Sutherland, P. and
890   Kuusela, M.: Summertime increases in upper-ocean stratification and mixed-layer depth, Nature 7851, 2021.

Scoccimarro, E., Gualdi, S., Bellucci, A., Sanna, A., Giuseppe Fogli, P., Manzini, E., Vichi, M., Oddo, P. and Navarra, A.: Effects of tropical cyclones on ocean heat transport in a high-resolution coupled general circulation model, J.Clim. 16, 2011.

Siahaan, A., Smith, R., Holland, P., Jenkins, A., Gregory, J. M., Lee, V., Mathiot, P., Payne, T., Ridley, J. and Jones, C.: The Antarctic contribution to 21st century sea-level rise predicted by the UK Earth System Model with an interactive ice sheet, The Cryosphere Discussions, 2021.

Silvano, A., Rintoul, S. R. and Herraiz-Borreguero, L.: Ocean-ice shelf interaction in East Antarctica, Oceanography 4, 2016.

Silvano, A., Rintoul, S. R., Peña-Molino, B., Hobbs, W. R., van Wijk, E., Aoki, S., Tamura, T. and Williams, G. D.: Freshening by glacial meltwater enhances melting of ice shelves and reduces formation of Antarctic Bottom Water, Science advances 4, 2018.

Smethie Jr, W. M. and Jacobs, S. S.: Circulation and melting under the Ross Ice Shelf: estimates from evolving CFC, salinity and temperature fields in the Ross Sea, Deep Sea Research Part I: Oceanographic Research Papers 6, 2005.

Smith, R. S., Mathiot, P., Siahaan, A., Lee, V., Cornford, S. L., Gregory, J. M., Payne, A. J., Jenkins, A., Holland, P. R. and Ridley, J. K.: Coupling the UK Earth System Model to dynamic models of the Greenland and Antarctic ice sheets, Journal of Advances in Modeling Earth Systems 10, 2021.

Solodoch, A., Stewart, A. L., Hogg, A. M., Morrison, A. K., Kiss, A. E., Thompson, A. F., Purkey, S. G. and Cimoli, L.: How Does Antarctic Bottom Water Cross the Southern Ocean? Geophys.Res.Lett. 7, 2022.

Storkey, D., Blaker, A. T., Mathiot, P., Megann, A., Aksenov, Y., Blockley, E. W., Calvert, D., Graham, T., Hewitt, H. T. and Hyder, P.: UK Global Ocean GO6 and GO7: A traceable hierarchy of model resolutions, Geoscientific Model Development 8, 2018.

Swart, N. C., Cole, J. N., Kharin, V. V., Lazare, M., Scinocca, J. F., Gillett, N. P., Anstey, J., Arora, V., Christian, J. R. and Hanna, S.: The Canadian earth system model version 5 (CanESM5. 0.3), Geoscientific Model Development 11, 2019.

Thompson, A. F., Stewart, A. L., Spence, P. and Heywood, K. J.: The Antarctic Slope Current in a changing climate, Rev.Geophys. 4, 2018.

van Caspel, M., Schröder, M., Huhn, O. and Hellmer, H. H.: Precursors of Antarctic Bottom Water formed on the continental shelf off Larsen Ice Shelf, Deep Sea Research Part I: Oceanographic Research Papers, 2015.

Vancoppenolle, M., Rousset, C., Blockley, E., and the NEMO Sea Ice Working Group. : SI3 – Sea Ice modelling Integrated Initiative – The NEMO Sea Ice Engine, 10.5281/zenodo.7534900, 2023.

Voldoire, A., Sanchez-Gomez, E., Salas y Mélia, D., Decharme, B., Cassou, C., Sénési, S., Valcke, S., Beau, I., Alias, A. and Chevallier, M.: The CNRM-CM5. 1 global climate model: description and basic evaluation, Clim.Dyn. 9, 2013.

Whitehead, J. A. : Dense water off continents, Nature 6124, 1987.

Williams, G. D., Herraiz-Borreguero, L., Roquet, F., Tamura, T., Ohshima, K. I., Fukamachi, Y., Fraser, A. D., Gao, L., Chen, H. and McMahon, C. R.: The suppression of Antarctic bottom water formation by melting ice shelves in Prydz Bay, Nature Communications 1, 2016.

Zweng, M. M., Seidov, D., Boyer, T. P., Locarnini, M., Garcia, H. E., Mishonov, A. V., Baranova, O. K., Weathers, K., Paver, C. R. and Smolyar, I.: World Ocean Atlas 2018, volume 2: Salinity, 2019.

Zweng, M.M, J.R. Reagan, J.I. Antonov, R.A. Locarnini, A.V. Mishonov, T.P. Boyer, H.E. Garcia, O.K. Baranova, D.R. Johnson, D.Seidov, M.M. Biddle. : World Ocean Atlas 2013, 2013.